arXiv:0709.4309v1 [astro-ph] 27 Sep 2007

# The Globular Cluster System of M60 (NGC 4649). II. Kinematics of the Globular Cluster System*

Ho Seong Hwang[1,5,6], Myung Gyoon Lee[1], Hong Soo Park[1], Sang Chul Kim[2],
Jang-Hyun Park[2], Young-Jong Sohn[3], Sang-Gak Lee[1], Soo-Chang Rey[4],
Young-Wook Lee[3], Ho-Il Kim[2]

## ABSTRACT

We present a kinematic analysis of the globular cluster (GC) system in the giant elliptical galaxy (gE) M60 in the Virgo cluster. Using the photometric and spectroscopic database of 121 GCs (83 blue GCs and 38 red GCs), we have investigated the kinematics of the GC system. We have found that the M60 GC system shows a significant overall rotation. The rotation amplitude of the blue GCs is slightly smaller than or similar to that of the red GCs, and their angles of rotation axes are similar. The velocity dispersions about the mean velocity and about the best fit rotation curve for the red GCs are marginally larger than those for the blue GCs. Comparison of observed stellar and GC velocity dispersion profiles with those calculated from the stellar mass profile shows that the mass-to-light ratio should be increased as the galactocentric distance increases, indicating the existence of an extended dark matter halo. The entire sample of GCs in M60 is found to have a tangentially biased velocity ellipsoid unlike the GC systems in other gEs. Two subsamples appear to have different velocity ellipsoids. The blue GC system has a modest tangentially biased velocity ellipsoid, while the

---

[1] Astronomy Program, Department of Physics and Astronomy, Seoul National University, 56-1 Sillim 9-dong, Gwanak-gu, Seoul 151-742, Korea

[2] Korea Astronomy and Space Science Institute, Daejeon 305-348, Korea

[3] Center for Space Astrophysics, Yonsei University, Seoul 120-749, Korea

[4] Department of Astronomy and Space Sciences, Chungnam National University, Daejeon 305-764, Korea

[5] hshwang@kias.re.kr

[6] Current address: Korea Institute for Advanced Study, Seoul 130-722, Korea

[7] *Based on observations obtained at the Canada-France-Hawaii Telescope (CFHT) which is operated by the National Research Council of Canada, the Institut National des Science de l'Univers of the Centre National de la Recherche Scientifique of France, and the University of Hawaii. This work is organized by the Korea Astronomy and Space Science Institute.

red GC system has a modest radially biased or an isotropic velocity ellipsoid. From the comparison of the kinematic properties of the M60 GC system to those of other gEs (M87, M49, NGC 1399, NGC 5128, and NGC 4636), it is found that the velocity dispersion of the blue GC system is similar to or larger than that of the red GC system except for M60, and the rotation of the GC system is not negligible. The entire sample of each GC system shows an isotropic velocity ellipsoid except for M60, while the subsamples show diverse velocity ellipsoids. We discuss the implication of these results for the formation models of the GC system in gEs.

*Subject headings:* galaxies: clusters: general — galaxies: individual (M60) — galaxies: kinematics and dynamics — galaxies: star clusters

## 1. Introduction

Globular Clusters (GCs) have been long recognized as an important tracer to understand the formation and evolution of galaxies. To solve the mystery of galaxy formation and evolution, several photometric properties of the GCs such as color distribution, spatial structure, and luminosity function have been used (Lee 2003; West et al. 2004; Brodie & Strader 2006). However, it is still difficult to test the predictions of the formation models of galaxies and their GC systems using photometric data alone.

Recently, with an aid of large telescopes with apertures larger than 4 meter, a large sample ($N > 150$) of GC spectra for one galaxy has been obtained, which can be used for statistically meaningful kinematic studies (e.g., Côté et al. 2001, 2003; Richtler et al. 2004; Peng et al. 2004). Due to their wide spatial distribution, brightness, and compact size, GCs are useful test particles to trace the gravitational potential of their host galaxies, and especially of the dark matter halo beyond several effective radii of the galaxy. Therefore, a kinematic study of the GC system enables us to estimate the global mass distribution of their host galaxy, or to constrain the orbital properties of GCs using an independently determined mass profile (e.g., from X-ray emission) of the galaxy. Moreover, the kinematic difference between GC subpopulations (blue and red GCs) can be used as an observational constraint on the galaxy formation model.

To date there are six giant elliptical galaxies (gEs) for which the kinematics of the GC system have been studied to our knowledge: M87 (Cohen & Ryzhov 1997; Kissler-Patig & Gebhardt 1998; Côté et al. 2001), M49 (Zepf et al. 2000; Côté et al. 2003), NGC 1399 (Kissler-Patig et al. 1998; Minniti et al. 1998; Kissler-Patig et al. 1999; Richtler et al. 2004), NGC 5128 (Peng et al.

2004; Woodley et al. 2007), NGC 4636 (Schuberth et al. 2006), and M60 (Bridges et al. 2006). M87, cD galaxy of the Virgo cluster, was studied recently by Côté et al. (2001) using $\sim$ 280 velocity data of GCs. The velocity dispersions of the blue and red GCs were found to be $\sim$410 km s$^{-1}$ and $\sim$390 km s$^{-1}$, respectively. Both the blue and red GCs appear to rotate around the photometric minor axis with a similar rotation amplitude of $\sim$ 160 km s$^{-1}$ when averaged over the whole system, while the blue GCs appear to rotate around the photometric major axis inside a radius of $\sim$ 16 kpc. The entire GC system has an isotropic velocity ellipsoid, while the blue and red GC systems show tangentially and radially biased one, respectively. Côté et al. (2003) studied the GC kinematics of M49, the brightest member of the Virgo cluster, using $\sim$ 260 velocity data of GCs. They found a larger velocity dispersion of the blue GCs ($\sim$350 km s$^{-1}$) than that of the red GCs ($\sim$270 km s$^{-1}$). The blue GCs rotate roughly around the photometric axis of M49 with a rotation amplitude of $\sim 100-150$ km s$^{-1}$, while the red GCs show some evidences for weak rotation ($\sim$ 50 km s$^{-1}$) around the same axis but a different direction. The entire, blue, and red GC systems appear to have an isotropic velocity ellipsoid. NGC 1399, cD galaxy of the Fornax cluster, was studied by Richtler et al. (2004) with the largest number ($\sim$ 470) of GC velocity data. The velocity dispersions of the blue and red GCs were estimated to be $\sim$291 km s$^{-1}$ and $\sim$255 km s$^{-1}$, respectively. No significant rotations were found for both the blue and red GCs, while there is a weak signature of rotation for blue GCs beyond $6'$. The velocity anisotropies for both the blue and red GCs are consistent with isotropic orbits. Using $\sim$ 220 GC data of NGC 5128, Peng et al. (2004) found that the red GCs exhibit a significant rotation, while the blue GCs do not show a clear hint of rotation. Later, Woodley et al. (2007), using 340 GC data for NGC 5128, showed that the rotation amplitude and the velocity dispersion for the subsamples are quite similar. For NGC 4636, Schuberth et al. (2006) found that the velocity dispersions of the blue and red GCs are not different, but the rotation of the red GCs is stronger than that of the blue GCs. In summary, all these GC systems show diverse GC kinematics in velocity dispersion, rotation, and their radial variation (see Section 4.1), making it difficult to draw any strong conclusion on the uniform formation history of the GC system in gEs.

M60 (NGC 4649) is a giant elliptical galaxy in the Virgo cluster, slightly less luminous than M87 and M49. M60 has a nearby companion Sc galaxy, NGC 4647, located at $2.'5$ from the center of M60. While there were numerous photometric studies of the GC system in M60 based on the ground-based images (Couture et al. 1991; Harris et al. 1991; Ashman & Zepf 1998; Forbes et al. 2004; Lee et al. 2007) and Hubble Space Telescope images (Neilsen 1999; Kundu & Whitmore 2001; Larsen et al. 2001; Peng et al. 2006; Strader et al. 2006; Mieske et al. 2006), there were few spectroscopic studies of the M60 GC system (Pierce et al. 2006). Pierce et al. (2006) published for the first time the spectroscopic observational results for 38 GCs (16 blue and 22 red GCs) in M60 using Gemini/GMOS. They found no obvious signs of a recent starburst, interaction or merger by estimating the ages and metallicities from the spectra of M60 GCs. Later, Bridges et al. (2006) investigated the kinematics of M60 GC system using the velocity data of Pierce et al. (2006). They reported that the velocity dispersion of the blue GCs is smaller than that of the red GCs unlike the cases of other gEs. They found no hint of rotation in the GC system of M60. Furthermore, orbital distribution of the GC system is found to be close to isotropic inside the radius of $100''$, but becomes tangentially biased beyond this radius. However, due to their small number ($N \sim 38$) of GC velocity data with limited radial and azimuthal coverage, it was difficult to derive the kinematic properties up to several effective radii, and to distinguish the kinematic difference between the blue and red GCs.

We have carried out a photometric study of the GC system in M60 using deep wide-field $CT_1$ images obtained at the KPNO 4m telescope (Lee et al. 2007), and a spectroscopic study using the spectra obtained at the Canada-France-Hawaii Telescope (CFHT) (Lee et al. 2006, Paper I). In this paper, we present the results of kinematic study of the GC system in M60 using the velocity data of 121 GCs selected in Paper I. Section 2 gives a brief description of the data used in this analysis, and the kinematic properties are derived in Section 3. From the comparison of kinematic properties of the M60 GC system to those of other gEs, we discuss our results regarding the GC formation models in Section 4. A summary of this study is given in the final section. We adopt a distance to M60, 17.3 Mpc, given by Mei et al. (2007) based on a surface brightness fluctuation method, and the corresponding scale for one arcmin is 5.032 kpc.

## 2. Data

We used the spectroscopic data of GCs given in Paper I, which describes the details of the spectroscopic observation, data reduction, and the data set. Here we only give a brief summary of the data set of M60 GCs.

We selected GC candidates in deep, wide-field Washington C and $T_1$ images ($16' \times 16'$) obtained at KPNO 4m telescope (Lee et al. 2007) and F555W (V) and F814W (I) images in the HST/WFPC2 archive data (Neilsen 1999; Kundu & Whitmore 2001; Larsen et al. 2001). Spectroscopic observations were made using the Multi Object Spectrograph (MOS) at the 3.6 m CFHT in February 2002 and in May 2003 for 165 GC candidates with $19 < T_1 < 22$ mag and $1.0 \leq (C - T_1) < 2.4$. We determined the radial velocities of GC candidates by cross-correlating the candidate spectrum with that of three Galactic GCs. Among 165 GC candidates, we could extract the spectra and determine the radial velocities for 111 objects, except for 54 objects due to the poor quality of their spectra. We increased the number of GCs by combining our data of radial velocities with those of Pierce et al. (2006). The radial velocities of GCs in Pierce et al. (2006) were transformed into our velocity system using equation (1) in Paper I, and the transformed velocities were used for further analysis. Of the entire spectroscopic sample of GC candidates (110 from Paper I and 38 from Pierce et al. 2006), 121 genuine GCs were selected in Paper I using a criteria of radial velocities ($500 \leq v_p \leq 1600$ km s$^{-1}$) and $(C - T_1)$ colors ($1.0 \leq C - T_1 < 2.4$ mag). There are 83 blue GCs with $1.0 \leq (C - T_1) < 1.7$ and 38 red GCs with $1.7 \leq (C - T_1) < 2.4$ in the total sample. Foreground reddening toward M60 is very small, $E(B - V) = 0.026$ (Schlegel et al. 1998), corresponding to $E(C - T_1) = 1.966E(B - V) = 0.051$, $A(T_1) = 0.071$, and $A(V) = 0.088$.

In Figure 1, we show the spatial distribution of 121 GCs in M60 with measured velocities. Two large dotted ellipses represent isophotes at the 25.0 B-mag arcsec$^{-2}$ of M60 (larger one) and NGC 4647 (smaller one) (de Vaucouleurs et al. 1991). It is worth noting that the majority of high velocity GCs (open symbols) with larger velocities than the systemic velocity of M60 (${v_{\rm gal}}^{1} = 1056 \pm 64$ km s$^{-1}$, Paper I), appear to be located to the north-west of M60. On the other hand, the majority of low velocity GCs (filled symbols) with smaller velocities than the systemic velocity of M60 appear to be located to the south-east of M60. It might be related to the overall rotation of the M60 GC system around the minor axis. However, a careful analysis is needed for further dynamical investigation due to the non-uniform spatial coverage of observed genuine GCs around M60.

## 3. Results

Using the master catalog of 121 GCs in M60 (Paper I), we have investigated the kinematic properties of the M60 GC system: the rotation amplitude, the position angle of the rotation axis, the mean line-of-sight velocity, the projected velocity dispersion, and the velocity ellipsoid.

### 3.1. Rotation of the Globular Cluster System

A detailed description of the relation between the intrinsic rotational velocity field and the projected one is given in Côté et al. (2001). In summary, if we assume that the GC

---

[1] $v_{\rm gal} = 1117 \pm 6$ km s$^{-1}$ in González (1993).

system is spherically symmetric with an intrinsic angular velocity field stratified on spheres, and that the GC rotation axis lies in the plane of the sky, then we can find that radial velocities of GCs depend sinusoidally on the azimuthal angles. For the M60 GC system, the assumption of spherical symmetry of the GC system is reasonable due to the modest projected ellipticity (effective ellipticity, $e_{\rm eff} = 0.21$, Lee et al. 2007). Therefore, we fit the observed line-of-sight velocities ($v_p$) of the GCs with the function,

$$v_p(\Theta) = v_{\rm sys} + (\Omega R)\sin(\Theta - \Theta_0) \ , \tag{1}$$

where $\Theta$ is the projected position angle of GCs relative to the galaxy center measured from north to east, $\Theta_0$ is the projected position angle of the rotation axis of the GC system, $R$ is the projected galactocentric distance, $(\Omega R)$ is the rotation amplitude, and $v_{\rm sys}$ is the systemic velocity of the GC system.

In Figure 2, we plot the radial velocities of GCs with measured uncertainties as a function of position angle for entire 121 GCs (top panel), 83 blue GCs (middle panel), and 38 red GCs (bottom panel). The best fit rotation curve of equation (1) for each sample is overlaid. The fitting was done using an error-weighted, nonlinear fit of equation (1) with $v_{\rm sys}$ as a fixed value of M60 recession velocity ($v_{\rm gal} = 1056 \pm 64$ km s$^{-1}$) rather than a free parameter for a better fitting. Using the biweight location of Beers et al. (1990), the systemic velocity of the M60 GC system is estimated to be $v_{\rm sys} = 1073^{+22}_{-22}$ km s$^{-1}$ (see Section 3.2), which agrees with the M60 recession velocity (1056±64 km s$^{-1}$) and the biweight mean velocity (1066±45 km s$^{-1}$) for 38 GCs given by Bridges et al. (2006) within the uncertainty. We derived the rotation amplitudes, $\Omega R$, $141^{+50}_{-38}$ km s$^{-1}$ for the entire GCs, $130^{+62}_{-51}$ km s$^{-1}$ for the blue GCs, and $171^{+58}_{-46}$ km s$^{-1}$ for the red GCs. Thus, the rotation amplitude of the blue GCs is slightly smaller than that of the red GCs, or is consistent with that of the red GCs within the uncertainty. Our results based on 121 GCs are in contrast to the fact that Bridges et al. (2006) found no rotation using only 38 GCs. To investigate the cause for difference of the rotation amplitudes between this study and Bridges et al. (2006), we estimate the rotation amplitude using all 121 GCs by dividing GCs into 54 GCs within the region of Bridges et al. (2006), and 67 GCs outside the region of Bridges et al. (2006). In the result, the rotation amplitude for the former sample is estimated to be $74^{+90}_{-27}$ km s$^{-1}$, which is much smaller than that for the latter sample ($\Omega R = 221^{+42}_{-41}$ km s$^{-1}$). Therefore, it is concluded that no rotation found in Bridges et al. (2006) is because of a small spatial coverage in their study.

In addition, the orientation of the rotation axis ($\Theta_0$) is estimated to be $225^{\circ}{}^{+12}_{-14}$ for the entire GCs, $218^{\circ}{}^{+16}_{-23}$ for the blue GCs, and $237^{\circ}{}^{+18}_{-19}$ for the red GCs. The orientations of rotation axes for all subsamples appear to be similar, and they are closer to the photometric minor axis ($\Theta_{phot} = 15^{\circ}$, or $195^{\circ}$, Lee et al. 2007) than the photometric major axis. Interestingly, the position angle of NGC 4647 relative to M60 is 314° from north to east. This means that the line connecting M60 and NGC 4647 is nearly perpendicular to the rotation axes of the GC system.

In Figure 3, we present the rotation of the GC system for the samples of different radial bins in order to investigate the radial variation of rotational properties. The top panel shows the GCs in the range of $32'' \leq R < 533''$, while the lower two panels show the GCs for the inner region ($32'' \leq R < 200''$, middle panel) and the outer region ($200'' \leq R < 533''$, bottom panel). The same fitting procedure used for the results in Figure 2 was applied for the entire, blue, and red GCs in each radial bin. The best fit rotation curves for each sample are overlaid as solid (entire GCs), dashed (blue GCs), and dotted (red GCs) lines.

It appears that the orientation of rotation axes for all GC subsamples changes slightly from the inner region to the outer region with a large uncertainty. The change of the rotation axis from the inner region to the outer region for the blue GCs is seen in the cases of M87 (Côté et al. 2001) and of M49 (Côté et al. 2003). The orientation of the rotation axis for the blue GCs in M87 drastically changes from the major axis in the inner region to the minor axis in the outer region. However, the blue GCs in M49 show the opposite change of rotation axis from the minor axis in the inner region to the major axis in the outer region. Due to the limited number of GCs in this study, it is difficult to make a solid conclusion on the radial change of the rotation axis for the M60 GC system. A larger sample of GCs is needed for further study on the change of the rotation axis as a function of the radius.

### 3.2. Velocity Dispersion of the Globular Cluster System

We summarize the kinematics of the M60 GC system derived in this study in Table 1. Several kinematic parameters for the entire, blue, and red GCs are presented for the entire region ($32'' \leq R < 533''$), the inner region ($32'' \leq R < 200''$), and the outer region ($200'' \leq R < 533''$). The column (1) defines the range of the projected radial distance from the center of M60 for each region in arcsec, and the column (2) gives the median value of the radial distance in arcsec. The number of GCs in each region is shown in the column (3). The column (4) and (5) represent the mean line-of-sight velocity (the biweight location of Beers et al. 1990) and the velocity dispersion about this mean velocity (the biweight scale of Beers et al. 1990), respectively. The position angle of the rotation axis and the rotation amplitude estimated using equation (1) in each region are given in the column (6) and (7), respectively. The column (8) gives the velocity dispersion about the best fit rotation curve. The column (9) gives the absolute value of the ratio of the rotation amplitude to the velocity dispersion about the best fit rotation curve. The uncertainties of these values represent 68% ($1\sigma$) confidence intervals that are determined from the numerical bootstrap procedure following the method of Côté et al. (2001). The estimated velocity dispersion for entire 121 GCs ($234^{+13}_{-14}$ km s$^{-1}$) agrees with the value ($256 \pm 29$ km s$^{-1}$) of Bridges et al. (2006) based on 38 GCs within the uncertainty. In addition, it is found that the velocity dispersion about the mean velocity of the GC system for the red GCs ($\sigma_p = 258^{+21}_{-31}$ km s$^{-1}$) is marginally larger than that for the blue GCs ($\sigma_p = 223^{+13}_{-16}$ km s$^{-1}$), which confirms the result of Bridges et al. (2006) with improved statistics. Interestingly, the velocity dispersion about the best fit rotation curve for the red GCs ($\sigma_{p,r} = 240^{+20}_{-34}$ km s$^{-1}$) is also marginally larger than that for the blue GCs ($\sigma_{p,r} = 207^{+15}_{-19}$ km s$^{-1}$).

In Figure 4, we plot the radial velocities of GCs with measured uncertainties against projected galactocentric distances. The mean radial velocities in two radial bins are overlaid by squares with long horizontal errorbar. The velocity dispersion about the mean velocity in each bin is also represented by a vertical errorbar. The mean velocities of all samples agree well with the systemic velocity of M60. Both of the velocity dispersions about the mean velocity and about the best fit rotation curve in the inner region are marginally larger than or comparable to those in the outer region for all three samples (see Table 1).

To investigate the radial variation of velocity dispersion in detail, we present a smoothed radial profile of velocity dispersions about the mean radial velocity (filled symbols) and about the best fit rotation curve (open symbols) in Figure 5. We calculate the velocity dispersion of the GCs lying within a bin with fixed radial width, $\Delta R = 120'' \simeq 10.06$ kpc as increasing the bin center by a fixed step width, $\delta R = 10'' \simeq 0.84$ kpc. We define the radial width and the step width so that the number of GCs per bin exceeds 10, and the calculation stops when the number of GCs in a bin is less than 10. The velocity dispersions about the mean radial velocity of the entire and blue GCs are nearly constant for the range of radius. However, velocity dispersions of the red GCs are decreasing in the inner region ($R \lesssim 18$ kpc) and are increasing in the outer region ($R \gtrsim 18$ kpc) although the variation is not large. The velocity dispersions about the best fit rotation curves of all three samples are not different from those about the mean radial velocities.

### 3.3. Velocity Anisotropy of the Globular Cluster System

If we assume the spherical symmetry of the M60 GC system, we can apply the Jeans equation in the absence of rotation to the dynamical analysis of the GC system. The spherical Jeans equation is

$$\frac{d}{dr}\, n_{\rm cl}(r)\sigma_r^2(r) + \frac{2\,\beta_{\rm cl}(r)}{r}\, n_{\rm cl}(r)\sigma_r^2(r) = -n_{\rm cl}(r)\,\frac{GM_{\rm tot}(r)}{r^2}\ , \tag{2}$$

where $r$ is a three dimensional radial distance from the galactic center, $n_{\rm cl}(r)$ is a three dimensional density profile of the GC system, $\sigma_r(r)$ is a radial component of velocity dispersion, $\beta_{\rm cl}(r) \equiv 1 - \sigma_\theta^2(r)/\sigma_r^2(r)$ is a velocity anisotropy, $G$ is the gravitational constant, and $M_{\rm tot}(r)$ is a total gravitating mass contained within a sphere of radius $r$ (e.g., Binney & Tremaine 1987). $\sigma_\theta(r)$ is a tangential component of velocity dispersion that is equal to an azimuthal component of the velocity dispersion, $\sigma_\phi(r)$, in a spherical case.

Several studies on the dynamics of the GC system have focused on determining the gravitational mass, $M_{\rm tot}(r)$, using the Jeans equation by assuming a simple isotropic orbit with $\beta_{\rm cl}(r) = 0$ (e.g., Cohen & Ryzhov 1997; Minniti et al. 1998; Zepf et al. 2000). However, with an aid of an independent determination of the mass profile of an elliptical galaxy using X-ray data (e.g., Brighenti & Mathews 1997; Humphrey et al. 2006 for M60), the velocity anisotropy itself can be investigated (e.g., Romanowsky & Kochanek 2001; Côté et al. 2001, 2003). Following the analysis of the M87 GC system by Côté et al. (2001) and the M49 GC system by Côté et al. (2003), we derive first the three dimensional density profile of the GC system, $n_{\rm cl}(r)$ and the total mass profile, $M_{\rm tot}(r)$. Comparing the velocity dispersion profile (VDP) calculated from the Jeans equation using those inputs with the measured VDP $\sigma_p(R)$, we determine the velocity anisotropy of the M60 GC system.

### *3.3.1. Density Profiles for the GC system*

We used the surface number density profiles of M60 GCs in Lee et al. (2007). They derived the surface density profile of M60 GCs by combining the HST/WFPC2 archive data for the inner region at $R < 1.5'$, and the KPNO data for the outer region at $R > 1.5'$. They determined the background levels from the mean surface number density of the point sources at $9' - 10'$ with the same range of magnitude and color as the GCs in the KPNO images: $1.988 \pm 0.363$ per square arcmin for the entire GCs, $1.790 \pm 0.344$ per square arcmin for the blue GCs, and $0.199 \pm 0.115$ per square arcmin for the red GCs. Then they subtracted these background values from the original number counts to produce the radial profiles of the net surface number density of GCs. Since they selected GCs that are brighter than $T_1 \approx 23.0$ mag[2], it is needed to correct the surface number density profile in order to account for the uncounted GCs due to the limiting magnitude. To calculate the correction factor, the equation (11) in McLaughlin (1999) with $V_{lim,1} = \infty$ was used on the assumption that the GC luminosity function of M60 has a Gaussian shape with a peak at $V \approx 23.8$ mag and a dispersion $\sigma = 1.65$ mag (Kundu & Whitmore 2001). It is found that the surface number density of the bright M60 GCs in Lee et al. (2007) should be multiplied by 2.61 to derive the total surface number density.

---

[2] This limiting magnitude corresponds to $V \approx 23.31$ mag using the transformation relation between $VI$ system and $CT_1$ system of Lee et al. (2007).

We display the total surface number density profiles, $N_{\rm cl}(R)$, for the entire, blue and red GCs in Figure 6. We fit the surface number density profile with the projection of Navarro et al. (1997, NFW) density profile, $n_{\rm cl}(r) = n_0(r/b)^{-1}(1 + r/b)^{-2}$ and with the projection of one of the galaxy models developed by Dehnen (1993), $n_{\rm cl}(r) = n_0(r/a)^{-\gamma}(1 + r/a)^{\gamma-4}$. The surface number density profile, $N_{\rm cl}(R)$, is related to the three dimensional density profile $n_{\rm cl}(r)$ as follows:

$$N_{\rm cl}(R) = 2\int_R^\infty n_{\rm cl}(r)\frac{r\,dr}{\sqrt{r^2 - R^2}}\ . \tag{3}$$

The solid and long dashed lines represent the projected best fit curves of the NFW profile and of the Dehnen profile, respectively. The fitting results for the entire (E) GCs, blue (B) GCs, and red (R) GCs are summarized as follows:

$$\begin{aligned} n_{\rm cl}^{\rm E}(r) &= 0.61\,{\rm kpc}^{-3}(r/5.96\,{\rm kpc})^{-1}(1 + r/5.96\,{\rm kpc})^{-2} \\ n_{\rm cl}^{\rm B}(r) &= 0.32\,{\rm kpc}^{-3}(r/6.07\,{\rm kpc})^{-1}(1 + r/6.07\,{\rm kpc})^{-2} \\ n_{\rm cl}^{\rm R}(r) &= 0.46\,{\rm kpc}^{-3}(r/4.99\,{\rm kpc})^{-1}(1 + r/4.99\,{\rm kpc})^{-2}, \end{aligned} \tag{4}$$

for the NFW profile, and

$$\begin{aligned} n_{\rm cl}^{\rm E}(r) &= 1.42\,{\rm kpc}^{-3}(r/7.97\,{\rm kpc})^{-0.29}(1 + r/7.97\,{\rm kpc})^{-3.71} \\ n_{\rm cl}^{\rm B}(r) &= 0.57\,{\rm kpc}^{-3}(r/8.75\,{\rm kpc})^{-0.40}(1 + r/8.75\,{\rm kpc})^{-3.60} \\ n_{\rm cl}^{\rm R}(r) &= 0.53\,{\rm kpc}^{-3}(r/8.36\,{\rm kpc})^{-0.56}(1 + r/8.36\,{\rm kpc})^{-3.44}, \end{aligned} \tag{5}$$

for the Dehnen profile.

It is found that the scale length $b$ of the red GCs in the NFW profile is smaller than that of the blue GCs, indicating that the red GCs are more concentrated toward the galaxy center than the blue GCs, as shown previously (Forbes et al. 2004; Lee et al. 2007).

### *3.3.2. Need for an Extended Dark Matter Halo in M60*

In the left panel of Figure 7, we plotted the surface brightness profile of M60 derived from our KPNO $T_1$-band images (Lee et al. 2007) compared to that in Peletier et al. (1990)

for the $R$-band photometry. We convert $T_1$ photometry of Lee et al. (2007) to Cousins $R$-band photometry using the relation given by Geisler (1996). It is seen that two profiles agree well over the radius.

We fit the surface brightness profile derived from the KPNO images (Kim et al. 2006; Lee et al. 2007) with the projection of three dimensional luminosity density profile used in Côté et al. (2003), which is represented by,

$$j(r) = \frac{(3-\gamma)(7-2\gamma)}{4} \frac{L_{\rm tot}}{\pi a^3} \left(\frac{r}{a}\right)^{-\gamma} \left[1 + \left(\frac{r}{a}\right)^{1/2}\right]^{2(\gamma-4)} . \tag{6}$$

The fit yields the parameters of $\gamma = 0.32$, $L_{\rm tot} = 1.32 \times 10^{11}\ L_{R,\odot}$, and $a = 1.48$ kpc, and the projected best fit curve is overlaid in Figure 7. The fitted model also gives an effective radius of $R_{\rm eff} = 1.'96 \simeq 9.86$ kpc, which is slightly larger than that from a fit ($R_{\rm eff} = 1.'83 \simeq 9.23$ kpc at $T_1$-band) using a de Vaucouleurs law in Lee et al. (2007).

In the right panel of Figure 7, we show a three dimensional stellar mass density profile, $\rho_s(r) = \Upsilon_0 j(r)$, with $R$-band mass-to-light ratio $\Upsilon_0 = 6.0\ M_\odot L_{R,\odot}^{-1}$ (discussed later in this Section). Thus we obtain a stellar mass profile of M60, which is represented by

$$\begin{aligned} M_{\rm s}(r) &= \int_0^r 4\pi x^2 \rho_s(r) dx = \Upsilon_0 \int_0^r 4\pi x^2 j(x) dx \\ &= \Upsilon_0 L_{\rm tot} \left[\frac{(r/a)^{1/2}}{1+(r/a)^{1/2}}\right]^{2(3-\gamma)} \left[\frac{(7-2\gamma)+(r/a)^{1/2}}{1+(r/a)^{1/2}}\right] . \end{aligned} \tag{7}$$

We used this stellar mass profile to determine the velocity anisotropy for the M60 stellar system and to test the existence of an extended dark matter halo. If we take $M_{\rm tot}(r) = M_{\rm s}(r)$ and substitute $n_{\rm cl}(r)$ by $\rho_s(r) \propto j(r)$, then we can compute the intrinsic radial VDP of the stars through the Jeans equation by assuming several $R$-band mass-to-light ratios ($\Upsilon_0$) and velocity anisotropies of the stellar system ($\beta_{\rm s}(r)$). We therefore predict the projected VDPs for the stellar system from the intrinsic radial VDP calculated using equation (10). In Figure 8, we show the projected VDPs calculated with $\Upsilon_0 = 6.0\ M_\odot L_{R,\odot}^{-1}$ and $\beta_{\rm s}(r) = +0.6$ (radially biased), which is the best fit curve for the stellar kinematic data of Fisher et al. (1995), de Bruyne et al. (2001), and Pinkney et al. (2003). This $R$-band mass-to-light ratio and radially biased velocity anisotropy for the stellar system is similarly found in the M49 stellar system with $\Upsilon_0 = 5.9\ M_\odot L_{R,\odot}^{-1}$ and $\beta_{\rm s}(r) = +0.3$ (Côté et al. 2003 and references therein).

For the comparison, we also present the projected VDPs calculated using the same stellar mass profile as above, but for the GC number density profile $n_{\rm cl}(r)$ and for $\beta_{\rm cl}(r) = +0.99$

(radially biased, upper long dashed lines), −99 (tangentially biased, lower long dashed lines), 0.0 (isotropic, solid line for the NFW profile and short dashed line for the Dehnen profile). Interestingly, none of these models can account for the observed VDPs for the GCs at $R > 7$ kpc, indicating that mass-to-light ratio is not constant over the galactocentric distance, but should be increased as the distance increases. This means that there exists an extended dark mater halo in M60. This result is consistent with the previous findings of an extended dark mater halo in M60 from a radial profile of an increasing mass-to-light ratio in $K$-band (Humphrey et al. 2006) and in $V$-band (Bridges et al. 2006) at $7 \lesssim R \lesssim 22$ kpc.

### *3.3.3. X-ray Mass Profile*

The total gravitating mass profile is determined using a gas temperature profile and a density distribution obtained from X-ray observational data on the assumption of hydrostatic equilibrium (neglecting magnetic pressure term):

$$M_{\rm tot}(r) = -\frac{kT(r)r}{G\mu m_p}\left(\frac{d\log\rho(r)}{d\log r} + \frac{d\log T(r)}{d\log r}\right), \tag{8}$$

where $k$ is the Boltzmann constant, $G$ is the gravitational constant, $T(r)$ is a gas temperature at radius $r$, $\mu$ is the mean molecular weight (taken as 0.63 in this study), $m_p$ is the proton mass, and $\rho(r)$ is a gas density at radius $r$. For the case of M60, Brighenti & Mathews (1997) derived the total mass profile using *Einstein* HRI observational data of Trinchieri et al. (1986) and *ROSAT* PSPC observational data of Trinchieri et al. (1997), and Humphrey et al. (2006) derived the total mass profile using *Chandra* observational data. In addition, Randall et al. (2006) reported the density and the temperature distribution of M60 using *XMM-Newton* data. Since the derived VDP is sensitive to the mass profile, we estimate mass profiles using these different X-ray data set.

In Figure 9, we display the deprojected profiles of the gas temperature (top panel) and the gas number densities (middle and bottom panels) found by Trinchieri et al. (1986, filled circles), Trinchieri et al. (1997, open circles), Randall et al. (2006, open triangles), and Humphrey et al. (2006, open stars) with measured errors. Having done this, we fit the temperature and gas number density data of each reference using the temperature distribution of $T(r) = 2T_m[r_m/(r+r_{ot})+(r/r_m)^q]^{-1}$, and the density distribution of $n(r) = \Sigma n_i(r)$, where $n_i(r) = n_0(i)[1 + \{r/r_0(i)\}^{p(i)}]^{-1}$. $T_m$, $r_m$, $r_{ot}$, $q$, $n_0(i)$, $r_0(i)$, and $p(i)$ are parameters of the fit. We fit the gas number density profile of each data for two cases of $i \leq 1$ (one component fit) and $i \leq 2$ (two component fit). The data in use are annotated with the associated lines. The results for the fit are summarized in Table 2.

The resulting mass profiles of M60, $M(r)$, for several temperature and gas number density profiles are presented in Figure 10. The upper panel shows the mass profiles using one component fit of the gas number density for various data set. The lower panel shows those using two components of the gas number density for various data set and using the mass profile derived by Humphrey et al. (2006) in comparison. It appears that most mass profiles agree well. However, the mass profile derived using the temperature and the gas number density data (with one component fit) of Trinchieri et al. (1997, the dotted line in the upper panel) deviates from the other profiles in the inner region ($r \leq 10$ kpc). In addition, the mass profile derived by Humphrey et al. (2006, the short dashed line in the lower panel) deviates from the other profiles in the region of $r \leq 1$ kpc. Comparing X-ray mass profiles with the stellar mass profile (heavy solid line) determined in §3.3.2, we find that most X-ray mass profiles deviate significantly from the stellar mass profiles in the inner region at $r < 2$ kpc, indicating that X-ray mass profiles are not reliable at the very small radius because of angular resolution limit and non-equilibrium energetics. In the intermediate region at $2 < r < 10$ kpc, the X-ray mass profiles derived using two component fit of the gas number density (lower panel) agree to the stellar mass profiles, while those derived using one component fit of the gas number density (upper panel) do not. In the outer region at $r > 10$ kpc, all X-ray mass profiles are larger than the stellar mass profiles, confirming the need of an extended dark matter halo as shown in §3.3.2. Since the discrepancy between X-ray and stellar mass profiles is significant only in the inner region at $r < 2$ kpc, where there are no GCs, and X-ray mass profiles that account for the dark matter halo are similar to or larger than the stellar mass profile at $r > 2$ kpc, we conclude that the X-ray mass profiles are good enough to determine the velocity anisotropy of the M60 GC system for the following analysis.

### *3.3.4. Determination of the Velocity Anisotropy*

We determine the velocity anisotropy of GCs as follows: (1) With the GC number density profile ($n_{\rm cl}(r)$) of the entire, blue, and red GCs and the mass profile ($M_{\rm tot}(r)$) in hand, assuming the velocity anisotropy ($\beta_{\rm cl}(r)$) in prior, we derive the theoretical projected VDP ($\sigma_p(R)$) and theoretical projected aperture VDP ($\sigma_{ap}(\leq R)$) using the Jeans equation; (2) From the comparison of these calculated VDPs with measured VDPs, we determine the velocity anisotropy of GCs.

We begin by deriving the theoretical projected VDPs. The equation (2), spherical Jeans equation can be solved for the radial component of velocity dispersion, $\sigma_r(r)$:

$$\sigma_r^2(r) = \frac{1}{n_{\rm cl}(r)} \exp\left(-\int \frac{2\beta_{\rm cl}}{r}\,dr\right) \left[\int_r^\infty n_{\rm cl}\,\frac{GM_{\rm tot}}{x^2} \exp\left(\int \frac{2\beta_{\rm cl}}{x}\,dx\right) dx\right] . \qquad (9)$$

Then the projected VDP, $\sigma_p(R)$ can be derived by

$$\sigma_p^2(R) = \frac{2}{N_{\rm cl}(R)} \int_R^\infty n_{\rm cl}\sigma_r^2(r) \left(1 - \beta_{\rm cl}\frac{R^2}{r^2}\right) \frac{r\,dr}{\sqrt{r^2 - R^2}}, \tag{10}$$

where $R$ is the projected galactocentric distance and the surface density profile, $N_{\rm cl}(R)$, is a projection of the three dimensional density profile $n_{\rm cl}(r)$. The projected aperture VDP, $\sigma_{\rm ap}(\leq R)$, which is the velocity dispersion of all objects interior to a given projected radial distance $R$, can be computed by

$$\sigma_{\rm ap}^2(\leq R) = \left[\int_{R_{\rm min}}^{R} N_{\rm cl}(R')\sigma_p^2(R')\,R'\,dR'\right]\left[\int_{R_{\rm min}}^{R} N_{\rm cl}(R')\,R'\,dR'\right]^{-1}, \tag{11}$$

where $R_{min}$ is the projected galactocentric distance of the innermost data point in the GC sample ($R_{min} = 2.7$ kpc in this study).

We present the measured VDP in comparison with the VDPs calculated by assuming several velocity anisotropies in Figures 11 and 12. Figure 11 shows the VDPs calculated using the Dehnen profile for the GC number density, while Figure 12 shows those using the NFW profile for the GC number density. The upper panels show the projected VDPs, and the lower panels show the projected aperture VDPs. The measured dispersion data taken from Figure 5 are shown by filled circles along with their confidence intervals. The projected aperture VDPs in the lower panels are plotted in the similar fashion to the case of the upper panel. The calculated VDPs in the left panels are obtained with the mass profiles derived using one component fit of the gas number density, while those in the right panels are obtained with the mass profiles derived using two component fit of the gas number density. Although it is difficult to distinguish the velocity anisotropy clearly for nearly all radial distances in the upper panel (the bottom panels show a more stable result), it appears that the entire GC system does not have an isotropic velocity ellipsoid ($\beta_{\rm cl} = 0$), but have a modest tangentially biased velocity ellipsoid ($\beta_{\rm cl} < 0$) for any mass profile in Figure 11 based on the Dehnen profile for the GC number density. A similar result can be found in Figure 12 based on the NFW profile for the GC number density. Bridges et al. (2006) reported that the orbits of M60 GCs are close to isotropic within $100''$ ($\sim$8.4 kpc) and becomes tangentially biased beyond $100''$. Our results appear to be consistent with those of Bridges et al. (2006) as a whole, although the signature of an isotropic orbit within $100''$ is weaker in this study. However, we extend the radial coverage ($\sim$21 kpc) of Bridges et al. (2006) out to $\sim$40 kpc in this study.

In Figures 13 and 14, we show a similar analysis for the blue and red GCs, respectively. We present the results using the Dehnen profile of GC number density for the blue and red GCs. The results using the NFW profile are not different from those in Figures 13 and 14.

Although it is not easy to draw a strong conclusion due to the small number statistics and complex mass profiles, we note a difference of velocity ellipsoids between the blue and red GCs in the projected aperture VDP (the bottom panels in Figure 13 and 14). It appears that the blue GC system has a tangentially biased velocity ellipsoid with $\beta_{\rm cl} < 0$, while the red GC system has a radially biased or an isotropic velocity ellipsoid.

## 4. Discussion

### 4.1. Comparison with the GC Systems in Other gEs

To date there are five giant elliptical galaxies except for M60 that the kinematics of their GC systems was studied: M87 (Cohen & Ryzhov 1997; Kissler-Patig & Gebhardt 1998; Côté et al. 2001), M49 (Zepf et al. 2000; Côté et al. 2003), NGC 1399 (Kissler-Patig et al. 1998; Minniti et al. 1998; Kissler-Patig et al. 1999; Richtler et al. 2004), NGC 5128 (Peng et al. 2004; Woodley et al. 2007), and NGC 4636 (Schuberth et al. 2006).

For the comparison of the kinematic properties of GCs in those gEs, we analyze the velocity data of 276 GCs in M87 (Côté et al. 2001), 263 GCs in M49 (Côté et al. 2003), 435 GCs in NGC 1399 (Richtler et al. 2004), 210 GCs in NGC 5128 (Peng et al. 2004), and 172 GCs in NGC 4636 (Schuberth et al. 2006) using the similar method adopted in this study. M87, M49, and NGC 4636 as well as M60 are gEs in the Virgo cluster, and NGC 1399 is a gE in the Fornax cluster at the similar distance to that of the Virgo cluster. NGC 5128 is in the Centaurus group, being the nearest gE. Basic photometric properties of these galaxies are listed in Table 3. The column (1), (2), and (3) give the name of galaxy, the absolute magnitude in the $V$ band, and the systemic radial velocity, respectively. The effective radius, the ellipticity, the position angle of photometric minor axis in degrees east of north, and the distance are shown in the column (4), (5), (6), and (7), respectively. The resulting global kinematics for the entire, blue and red GCs of each galaxy are presented in Table 4: the mean radial velocity, velocity dispersion about the mean radial velocity, rotation axis, rotation amplitude, rotation-corrected velocity dispersion, and the absolute value of the ratio of the rotation amplitude to the velocity dispersion about the best fit sine curve for each GC subsample. We divide the GCs in each gE into the blue and red GCs using the colors that were used in the associated reference, excluding the GCs without color information, for the kinematic analysis. In addition, we estimate the rotation amplitude and the position angle of rotation axis for the GC system of NGC 5128, by fitting the mean velocity of GCs lying in a fixed width (60 deg) of position angle for a stable computation. The velocity dispersions derived in this study agree well with those derived in the associated reference. The velocity dispersions of GCs in M87 ($\sigma_p = 414^{+15}_{-18}$ km s$^{-1}$) and NGC 1399

($\sigma_p = 323^{+11}_{-13}$ km s$^{-1}$) are found to be larger than and comparable to that of GCs in M49 ($\sigma_p = 322^{+14}_{-17}$ km s$^{-1}$), respectively, although M87 and NGC 1399 are fainter than M49. This is due to the fact that M87 and NGC 1399 are located in the center of a galaxy cluster, while M49 is not. NGC 5128 shows the smallest velocity dispersion ($\sigma_p = 129^{+5}_{-7}$ km s$^{-1}$) among our sample galaxies, implying a relatively smaller mass in spite of its high luminosity in the $V$ band ($M_V = -21.7$).

Table 5 lists several notable features based on the global kinematics presented in Table 4. The strength of rotation is defined in the column (4): strong for $\Omega R/\sigma_{p,r} > 0.4$, modest for $0.4 \geq \Omega R/\sigma_{p,r} > 0.2$, and weak for $\Omega R/\sigma_{p,r} \leq 0.2$. The rotation axis in the column (5) is assigned if the difference between the position angle of rotation axis and that of photometric major/minor axis is less than 30°. The result of velocity anisotropy for each GC system is taken from the literature (see column (6)). It appears that the rotation-corrected velocity dispersion, $\sigma_{p,r}$ of the blue GCs is similar to or larger than that of the red GCs except for M60. This implies that the blue GC system is dynamically hotter than the red GC system in most gEs. However, the case of rotation ($\Omega R/\sigma_{p,r}$) is not simple. Both of the blue and red GCs in M60 and M87 show a strong rotation, while those in NGC 1399 show a weak rotation. The red GCs in NGC 4636 and NGC 5128 show a slightly stronger rotation than the blue GCs. However, the red GCs in M49 show a weak rotation, while the blue GCs show a modest rotation, which is consistent with the prediction of the merger formation model (Ashman & Zepf 1992). In addition, if we consider the position angle of rotation axis together, the story becomes more complicated. In velocity anisotropy, it appears that the entire sample of the GC system in three gEs (M87, M49, and NGC 1399) has an isotropic velocity ellipsoid and two subsamples have different velocity ellipsoids in two gEs (M60 and M87). It is needed to determine the velocity anisotropy of the GC systems in more gEs including NGC 5128 and NGC 4636.

To examine the general kinematic properties of the GC systems in gEs, we plot the rotation-corrected velocity dispersions in gEs against the projected galactocentric distances in Figure 15. The rotation-corrected velocity dispersion is normalized by that of the entire GCs in each gE. The projected galactocentric distance is normalized by the effective radius of each gE. The entire and blue GCs do not show significant change of the velocity dispersion over the whole region of a galaxy. However, the velocity dispersion of the red GCs in the inner region ($R < 2R_{\rm eff}$) is, in the mean, marginally larger than that in the outer region ($R > 2R_{\rm eff}$). This implies that red GC system in the inner region may be dynamically hotter than that in the outer region. In Figure 16, the absolute value of the ratio of the rotation amplitude to the velocity dispersion is plotted as a function of the projected galactocentric distance. For the red GCs, the ratio of the rotation amplitude to the velocity dispersion in the outer region appears to be marginally larger than that in the inner region if we neglect the point of NGC 4636 (filled pentagon), while it does not change with the distance for the entire and blue GCs.

In summary, differences in kinematic properties among GC subsamples appear to exist, although it depends on the galaxy. The blue GC system appears to be dynamically similar to or hotter than the red GC system, while the rotation of the GC system is not negligible. The entire sample of each GC system appears to have an isotropic velocity ellipsoid, while the subsamples do not have uniform velocity ellipsoids. The kinematic properties of M60 and M87 are similar except for the velocity dispersion of subsamples and the velocity anisotropy of the entire GC system, while other galaxies have diverse kinematic properties. For the red GCs, the velocity dispersion of the inner region is marginally larger than that of the outer region, while the rotation of the outer region appears to be more significant than that of the inner region.

## 4.2. Formation Models of Globular Clusters

The kinematic properties of the GC system in M60 compared to those in other gEs are useful to test the kinematic predictions of formation models of the GCs in gE. A summary of several model descriptions and predictions can be found in several literature (Rhode & Zepf 2001; Lee 2003; Richtler et al. 2004; West et al. 2004; Brodie & Strader 2006). Classical formation models can be divided into four broad categories: the monolithic collapse model, the major merger model, the multiphase dissipational collapse model, and the dissipationless accretion model.

The monolithic collapse model describes that an elliptical galaxy and its GCs are formed through the collapse of an isolated massive gas cloud or protogalaxy at high redshift (Larson 1975; Carlberg 1984; Arimoto & Yoshii 1987). In this model, the color distribution of GCs shows a smooth shape with a single peak, and the rotation of GCs can be generated by tidal torques from companions (Peebles 1969). Although this model can explain some observational properties of elliptical galaxies successfully (see Chiosi & Carraro 2002), the bimodal color distribution of the GC system in many gEs (e.g., Lee 2003; Peng et al. 2006) make it hard to accept this model. In addition, the strong rotation of the GC system as seen in M60 and M87 is not expected from the collapse of a single, isolated protogalactic cloud. Moreover, several GC systems in gEs show a globally isotropic velocity ellipsoid that needs some kinds of relaxation processes that the monolithic collapse model can not account for.

The major merger model suggests that elliptical galaxies are formed by a merger of two or more disk galaxies (Toomre 1977; Ashman & Zepf 1992; Zepf et al. 2000). In this model, younger, spatially concentrated, red GCs are formed during the merger, while spatially extended, blue GCs come from the halos of the disk galaxies (e.g., Bekki et al. 2002). As a result, the color distribution of GCs is expected to be bimodal. This model predicts that the newly formed red GCs show little rotation compared to the blue GCs since the angular momentum would be transported to the outer region during the merging process. This model has received particular attention since it could explain several photometric properties of the GC system in gEs and little rotation of the red GC system in M49 (Zepf et al. 2000). However, contrary to the case of M49, the red GC system in M60, M87, NGC 5128, and NGC 4636 show a strong or modest rotation. From the simulation of dissipationless major mergers of spiral galaxies, Bekki et al. (2005) found that both pre-existing metal-poor clusters (MPCs) and metal-rich clusters (MRCs) obtain significant amounts of rotation beyond $\sim$ 10 kpc, regardless of the orbital configuration of the merging galaxies. However, both the blue and red GC systems in NGC 1399 show weak rotation, which is not consistent with the result of Bekki et al. (2005). Therefore, it is needed to explain what makes the complex rotational properties of the GC systems in gEs. In the dissipationless major merger model, most GCs are formed before a last major merger event. There are several observational results based on the spectroscopy of the GCs in gEs consistent with this: the blue GCs and red GCs show a small age difference and are both old : M60 (Pierce et al. 2006), M87 (Cohen et al. 1998), M49 (Beasley et al. 2000; Cohen et al. 2003), and NGC 1399 (Kissler-Patig et al. 1998; Forbes et al. 2001). Then, what we observe today is the GC system that was affected by the orbital mixing caused by the last major merger event, and the observed kinematics can not reflect the circumstance when the GC system was formed. Therefore, it is noted that it is difficult to trace the orbital history of the GC system from the observed kinematics (Kissler-Patig & Gebhardt 1998), and to test the validity of the dissipationless merger scenario.

Forbes et al. (1997) proposed the multiphase dissipational collapse model that ellipticals form their GCs in distinct star formation phases through a dissipational collapse. In addition, there is a capture of additional GCs by tidal effects from neighboring galaxies or the accretion of dwarf galaxies. Since the blue GCs are formed in the first star formation phase and the red GCs are formed in the subsequent star formation phase after the gas in the galaxy is self-enriched, the color distribution of GCs is expected to be bimodal. This model predicts that the blue GC system shows no rotation and a high velocity dispersion, while the red GC system shows some rotation depending on the degree of dissipation in the collapse. As the galactocentric distance increases up to $90''$, the stellar velocity dispersion in M60 approaches to the value of 200 km $s^{-1}$ (de Bruyne et al. 2001) that is comparable to or smaller than the velocity dispersion of the blue GCs. This might support this model, as Forbes et al. (1997) pointed out in the case of NGC 1399 and M87. However, this model disagrees with the results that blue GC systems in several gEs including M60 in Table 5 show larger than or comparable rotation amplitude to that of the red GC system.

Côté et al. (1998) proposed the dissipationless accretion model; the red GCs formed in a dissipational collapse, while the blue GCs were subsequently captured from other galaxies through mergers or tidal stripping. This model predicts a bimodal color distribution of GCs in gEs and a uniform color distribution in dwarf ellipticals. However, there is an example of low-luminosity elliptical galaxy (e.g., NGC 1427) that shows a bimodal color distribution (Forte et al. 2001). Since the blue GCs are captured from other galaxies, they are expected to show extended spatial distribution. Richtler et al. (2004) argued that if the scenario of Côté et al. (1998) is correct, then the blue GCs are expected to have radially biased orbits rather than the isotropic or tangentially biased orbits, and are also expected to show no rotation. Although the kinematic data for the outer GCs are not complete to date, current data for the blue GCs in Table 5 show negligible rotations and no signs of radially biased orbits, which is not consistent with the scenario of Côté et al. (1998).

Since the classical models do not give quantitative predictions concerning the kinematic properties of the GC system, it is instructive to compare the observational results with those in the recent numerical simulations. Although there are some numerical simulations of the GC system focusing on the color distribution (Beasley et al. 2002), the spatial distribution (Moore et al. 2006; Bekki & Forbes 2006), and the mass-metallicity relation for the blue GCs (Bekki et al. 2007), there are few simulation results that can be compared directly with observational results summarized in Table (Bekki et al. 2005; Kravtsov & Gnedin 2005)

In a pioneering work, Bekki et al. (2005) numerically investigated the kinematics of the GC system in E/S0 galaxies formed from a dissipationless merging of spiral galaxies. They presented the kinematic properties such as rotation and velocity dispersion of the pre-existing MPCs and MRCs for several merger configurations (e.g., pair and multiple mergers). For the rotation, both MPCs and MRCs show larger rotation amplitudes in the outer region ($R > 2R_{\rm eff}$) than those in inner region ($R \sim R_{\rm eff}$), regardless of the merger configuration. Interestingly, observational data in Figure 16 show that the rotation amplitudes for the blue GCs do not change as the galactocentric distance increases. However, those for the red GCs increase marginally from the inner region to the outer region if we neglect the point of NGC 4636 (filled pentagon), as expected in the simulation. For the velocity dispersion, the MPCs show slightly larger the central velocity dispersion than the MRCs, indicating that the MPCs are dynamically hotter than the MRCs. Moreover, the VDPs for both MPCs and MRCs are decreasing as the galactocentric distance increases in all major merger models, while those are sometimes very flat in multiple merger models. The kinematic data in Figure 15 show that the VDPs might be different depending on the galaxy (e.g., flat for M49 and increasing for M87), and the difference of VDPs between blue and red GCs appears to exist. Although the latter is not expected in the simulation, the former is consistent with the simulation, implying different merger histories depending on the galaxies.

Kravtsov & Gnedin (2005) studied the formation of the GCs in a Milky Way-size galaxy using a gas dynamics cosmological simulation with an adaptive refinement tree code. However, they had to stop the simulation at $z \sim 3.3$ due to the limited computational resources. Later, Gnedin & Prieto (2006), using a separate collisionless $N$-body simulation described in Kravtsov et al. (2004) up to $z = 0$, calculated the GC orbits for the similar galactic system. They found that, at present, the GC orbits are isotropic in the inner 50 kpc region from the galactic center, but radial in the outer region. Although it is difficult to exam the observational data at large distance ($> 50$ kpc) because of insufficient GC samples at that region, the isotropic orbit in the inner region is roughly consistent with the kinematic data of gEs (see Table 5).

On the other hand, Vesperini et al. (2003) modeled a dynamical evolution of the M87 GC system with different initial conditions for the mass function, the spatial distribution, and the velocity anisotropy of the GC system, following the evolution of a model GC system given by Vesperini (2000, 2001). In their result, for a two-slope power-law initial mass function of the GCs corresponding to the mass function of the old clusters, a flat radial profile for the mean mass of the GCs obtained from the observation can be acquired from the simulation with any velocity anisotropy of the GC system. However, for a power-law initial mass function of the GCs that is regarded as that of the young clusters, the observed flat radial profile for the mean mass of the GCs can be obtained from the simulation only with a strong radial anisotropy of the GC system. This initial radial anisotropy is much more radially biased than the observed one in the GC systems of gEs (having mostly isotropic velocity ellipsoids as seen in Table 5), raising a problem for a scenario that the young GC system in mergers like the Antennae may evolve into the GC system seen in gEs.

By viewing the formation of the M60 GC system in the context of kinematic predictions of above models, the strong rotations of the blue and red GC system are consistent with the simulation of Bekki et al. (2005). However, the larger velocity dispersion of the red GCs compared to the blue GCs in M60 is not consistent with the predictions of several formation models. M60 might be a particular case among gEs due to a possible interaction with the companion galaxy, NGC 4647. While they were regarded as a non-interacting system (e.g., Sandage & Bedke 1994), recent observational results suggest evidences of current interaction between two: (1) the morphological structure of NGC 4647 is clearly asymmetric (Koopman et al. 2001); (2) the stellar kinematic study shows that the inner region of M60 has a strong rotational support compared to other gEs, and has an asymmetric rotation curve (Pinkney et al. 2003; de Bruyne et al. 2001); (3) an X-ray filament that extends to the north-eastern edge of M60 is seen (Randall et al. 2006). (4) young luminous star clusters or associations in NGC 4647 are found (Lee et al. 2007). However, Pierce et al. (2006) found no obvious signs of a recent starburst, interaction or merger by estimating the ages and metallicities from the spectra of M60 GCs. Thus, it appears that the interaction between two started very recently, and did not affect the old M60 GC system significantly. The spatial coverage of observed GCs in Pierce et al. (2006) is not enough to study the interacting region between M60 and NGC 4647 (see Figure 1). Therefore, to understand the formation of M60 GC system in terms of an interaction between galaxies, it is important to obtain a large spectroscopic sample of GCs at larger galactocentric distance with high S/N ratio enough to determine the age and metallicity.

## 5. Summary

Using the photometric and spectroscopic database of 121 GCs (83 blue GCs and 38 red GCs) in the gE M60 (NGC 4649) in the Virgo cluster, we have investigated the kinematics of the GC system of this galaxy. Our primary results are summarized below:

1. Similar to the case of M87 GCs (Côté et al. 2001), the entire, blue and red GC subsamples of M60 show significant overall rotations. The rotation axes are nearly perpendicular to the line connecting M60 and its companion NGC 4647.

2. Both of the velocity dispersion about the mean velocity and about the best fit rotation curve of the red GCs are marginally larger than those of the blue GCs. This implies that the red GC system might be dynamically hotter than the blue GC system unlike the GC systems in other gEs.

3. Comparison of observed stellar and GC velocity dispersion profiles with those calculated from the stellar mass profile showed that the mass-to-light ratio is not constant, but should be increased as the galactocentric distance increases, indicating the existence of an extended dark matter halo in M60.

4. Using the X-ray mass profile, the number density distribution of GCs, and the observed VDP of GCs, we have determined the velocity ellipsoids of the M60 GC system. The entire GC system in M60 appears to have a tangentially biased velocity ellipsoid unlike the GC systems in other gEs. Two subsamples have a different velocity anisotropy: the blue GCs show a modest tangentially biased velocity ellipsoid, while the red GCs show a modest radially biased or an isotropic velocity ellipsoid.

5. We have compared the kinematics of the M60 GC system in this study with the results of other GC systems in gEs. As a whole, the rotation-corrected velocity dispersion of the blue GCs is similar to or larger than that of the red GCs unlike the M60 GC system. The rotation of the GC system in gEs is not negligible in contrast to the traditional view, though the details of rotation amplitudes and rotation axes need to be investigated further. The entire sample of each GC system appears to have an isotropic velocity ellipsoid, while the subsamples do not show unified velocity anisotropy.

In conclusion, the GC systems in gEs have common kinematic properties such as velocity dispersion, while the rotation and the velocity anisotropy show diverse results. These kinematic properties are not fully explained by any current models. We need extensive kinematic studies of other GC systems over larger galactocentric distances with various environmental effects to understand the diversity of the kinematics, and the formation and evolution of the GC system in gE. Moreover, it is desirable to have more elaborate model predictions for the kinematics of the GC system in gE including the velocity anisotropy.

We would like to thank anonymous referee for useful comments. The authors are grateful to the staff members of the CFHT for their warm support during our observations. M.G.L. is in part supported by the ABRL (R14-2002-058-01000-0).

## REFERENCES

Arimoto N., & Yoshii Y. 1987, A&A, 173, 23

Ashman, K.M., & Zepf, S.E. 1992, ApJ, 384, 50

Ashman, K.M., & Zepf, S.E. 1998, Globular Cluster Systems (Cambridge: Cambridge University Press)

Beasley, M. A., Sharples, R. M., Bridges, T. J., Hanes, D. A., Zepf, S. E., Ashman, K. M., & Geisler, D. 2000, MNRAS, 318, 1249

Beasley, M. A., Baugh, C. M., Forbes, D. A., Sharples, R. M., & Frenk, C. S. 2002, MNRAS, 333, 383

Beers, T. C., Flynn, K., & Gebhardt, K. 1990, AJ, 100, 32

Bekki, K., Forbes, D. A., Beasley, M. A., & Couch, W. J. 2002, MNRAS, 335, 1176

Bekki, K., Beasley, M. A., Brodie, J. P., & Forbes, D. A. 2005, MNRAS, 363, 1211

Bekki, K., & Forbes, D. A. 2006, A&A, 445, 485

Bekki, K., Yahagi, H., & Forbes, D. A. 2007, MNRAS, 377, 215

Binney, J., & Tremaine, S. 1987, Galactic Dynamics (Princeton: Princeton Univ. Press)

Bridges, T., et al. 2006, MNRAS, 373, 157

Brighenti, F., & Mathews, W. G. 1997, ApJ, 486, L83

Brodie, J. P., & Strader, J. 2006, ARA&A, 44, 193

Carlberg, R. G. 1984, ApJ, 286, 403

Chiosi, C., & Carraro, G. 2002, MNRAS, 335, 335

Cohen, J. G., & Ryzhov, A. 1997, ApJ, 486, 230

Cohen, J. G., Blakeslee, J. P., & Ryzhov, A. 1998, ApJ, 496, 808

Cohen, J. G., Blakeslee, J. P., & Côté, P. 2003, ApJ, 592, 866

Côté, P., Marzke, R.O., & West, M.J. 1998, ApJ, 501, 554

Côté, P., et al. 2001, ApJ, 559, 828

Côté P., McLaughlin D. E., Cohen J. G., Blakeslee J. P. 2003, ApJ, 591, 850

Couture, J., Harris, W. E., & Allwright, J. W. B. 1991, ApJ, 372, 97

de Vaucouleurs, G., de Vaucouleurs, A., Corwin, H. G. Jr., Buta, R. J., Paturel, H. G., & Fouqué, P. 1991, Third Reference Catalog of Bright Galaxies (New York: Springer)

de Bruyne, V., Dejonghe, H., Pizzella, A., Bernardi, M., & Zeilinger, W. W. 2001, ApJ, 546, 903

Dehnen, W. 1993, MNRAS, 265, 250

Dufour, R. J., Harvel, C. A., Martins, D. M., Schiffer, F. H., III, Talent, D. L., Wells, D. C., van den Bergh, S., & Talbot, R. J., Jr. 1979, AJ, 84, 284

Fisher, D., Illingworth, G., & Franx, M. 1995, ApJ, 438, 539

Forbes D.A., Brodie J.P., & Grillmair C.J. 1997, AJ, 113, 1652

Forbes, D. A., Beasley, M. A., Brodie, J. P., & Kissler-Patig, M. 2001, ApJ, 563, L143

Forbes D.A., et al. 2004, MNRAS, 355, 608

Forte J.C., Geisler D., Ostrov P., Piatti, A.E., & Gieren, W. 2001, AJ, 121, 1992

Geisler, D. 1996, AJ, 111, 480

Gnedin, O. Y., & Prieto, J. L. 2006, (astro-ph/0606169)

González, J. J., 1993, PhD thesis, Univ. California, Santa Cruz

Harris, W. E., Allwright, J. W. B., Pritchet, C. J., & van den Bergh, S. 1991, ApJS, 76, 115

Hui, X., Ford, H. C., Freeman, K. C., & Dopita, M. A. 1995, ApJ, 449, 592

Humphrey, P. J., Buote, D. A., Gastaldello, F., Zappacosta, L., Bullock, J. S., Brighenti, F., & Mathews, W. G. 2006, ApJ, 646, 899

Kim, E., Kim, D.-W., Fabbiano, G., Lee, M. G., Park, H. S., Geisler, D., & Dirsch, B. 2006, ApJ, 647, 276

Kissler-Patig, M., Brodie, J.P., Schroder, L.L., Forbes, D.A., Grillmair, C.J., & Huchra, J.P. 1998, AJ, 115, 105

Kissler-Patig, M., & Gebhardt, K. 1998, AJ, 116, 2237

Kissler-Patig M., Grillmair C.J., Meylan G., Brodie, J.P., Minniti, D., & Goudfrooij, P. 1999, AJ, 117, 1206

Koopman, R.A., Kenney, J.D.P., & Young, J. 2001, ApJS, 135, 125

Kravtsov, A. V., Gnedin, O. Y., & Klypin, A. A. 2004, ApJ, 609, 482

Kravtsov, A. V., & Gnedin, O. Y. 2005, ApJ, 623, 650

Kundu, A., & Whitmore, B.C. 2001, AJ, 121, 2950

Larsen, S.S., Brodie, J.P., Huchra, J.P., Forbes, D.A., & Grillmair, C.J. 2001, AJ, 121, 2974

Larson R.B. 1975, MNRAS, 173, 671

Lee, M. G. 2003, J. Korean Astro. Soc., 36, 189

Lee, M. G., et al. 2006, ApJ, submitted (Paper I)

Lee, M. G., Park, H. S., Kim, E., Hwang, H. S., Kim, S. C., & Geisler, D. 2007, ApJ, submitted

McLaughlin, D.E. 1999, AJ, 117, 2398

Mei, S., et al. 2007, ApJ, 655, 144

Mieske, S., et al. 2006, ApJ, 653, 193

Minniti, D., Kissler-Patig, M., Goudfrooij, P., & Meylan, G. 1998, AJ, 115, 121

Moore, B., Diemand, J., Madau, P., Zemp, M., & Stadel, J. 2006, MNRAS, 368, 563

Navarro, J. F., Frenk, C. S., & White, S. D. M. 1997, ApJ, 490, 493

Neilsen, E. H., Jr. 1999, Ph.D. Thesis, Johns Hopkins Univ.

Peebles, P. J. E. 1969, ApJ, 155, 393

Peng, E. W., Ford, H. C., & Freeman, K. C. 2004, ApJ, 602, 705

Peng, E. W., et al. 2006, ApJ, 639, 95

Pierce, M., et al. 2006, MNRAS, 368, 325

Pinkney, J., et al. 2003, ApJ, 596, 903

Peletier, R. F., Davies, R. L., Illingworth, G. D., Davis, L. E., & Cawson, M. 1990, AJ, 100, 1091

Randall, S.W., Sarazin, C.L., & Irwin, J.A. 2006, ApJ, 636, 200

Richtler, T., et al. 2004, AJ, 127, 2094

Rhode K.L., & Zepf S.E. 2001, AJ, 121, 210

Romanowsky, A. J., & Kochanek, C. S. 2001, ApJ, 553, 722

Sandage, A., & Bedke, J. 1994, The Carnegie Atlas of Galaxies (Washington: Carnegie Inst.)

Schlegel, D.J., Finkbeiner, D.P., & Davis, M. 1998, ApJ, 500, 525

Schuberth, Y., Richtler, T., Dirsch, B., Hilker, M., Larsen, S. S., Kissler-Patig, M., & Mebold, U. 2006, A&A, 459, 391

Smith, R. J., Lucey, J. R., Hudson, M. J., Schlegel, D. J., & Davies, R. L. 2000, MNRAS, 313, 469

Strader, J., Brodie, J. P., Spitler, L., & Beasley, M. A. 2006, AJ, 132, 2333

Tonry, J. L., et al. 2001, ApJ, 546, 681

Toomre, A. 1977, in The Evolution of Galaxies and Stellar Populations, ed. B. Tinsley & R. Larson (New Haven: Yale Univ. Obs.)

Trinchieri, G., Fabbiano, G., & Canizares, C. R. 1986, ApJ, 310, 637

Trinchieri, G., Fabbiano, G., & Kim, D-W. 1997, A&A, 318, 361

Vesperini, E. 2000, MNRAS, 318, 841

Vesperini, E. 2001, MNRAS, 322, 247

Vesperini, E., Zepf, S. E., Kundu, A., & Ashman, K. M. 2003, ApJ, 593, 760

West, M. J., Côté, P., Marzke, R. O., & Jordan, A. 2004, Nature, 427, 31

Woodley, K. A., Harris, W. E., Beasley, M. A., Peng, E. W., Bridges, T. J., Forbes, D. A., & Harris, G. L. H. 2007, AJ, 134, 494

Zepf, S.E., Beasley, M.A., Bridges, T.J., Hanes, D.A., Sharples, R.M., Ashman, K.M., & Geisler, D. 2000, AJ, 120, 2928

---

This preprint was prepared with the AAS LaTeX macros v5.2.

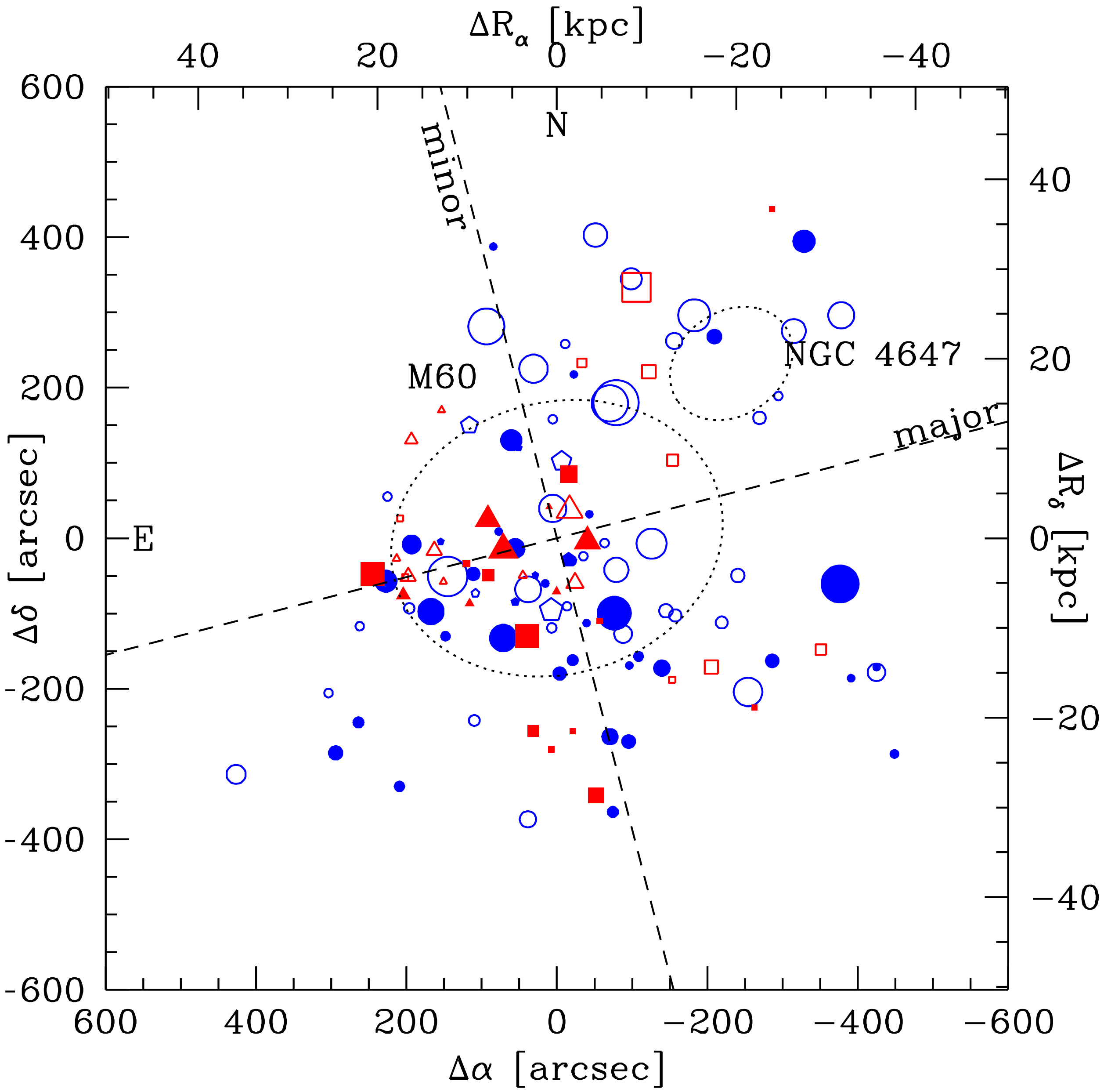

Fig. 1.— Spatial distribution of M60 GCs with measured velocities. The blue GCs measured in Paper I are represented by circles and those from Pierce et al. (2006) are represented by pentagons. The squares and triangles indicate the red GCs measured in Paper I and Pierce et al. (2006), respectively. The GCs with larger velocities than the systemic velocity ($v_{gal}$ = 1056 km $s^{-1}$) of M60 are plotted by open symbols, while those with smaller velocities than the systemic velocity of M60 by filled symbols. The symbol size is proportional to the velocity deviation. M60 and its companion galaxy, NGC 4647, are shown by large dotted $D_{25}$ ellipses. The photometric major and minor axes of M60 are represented by the dashed lines.

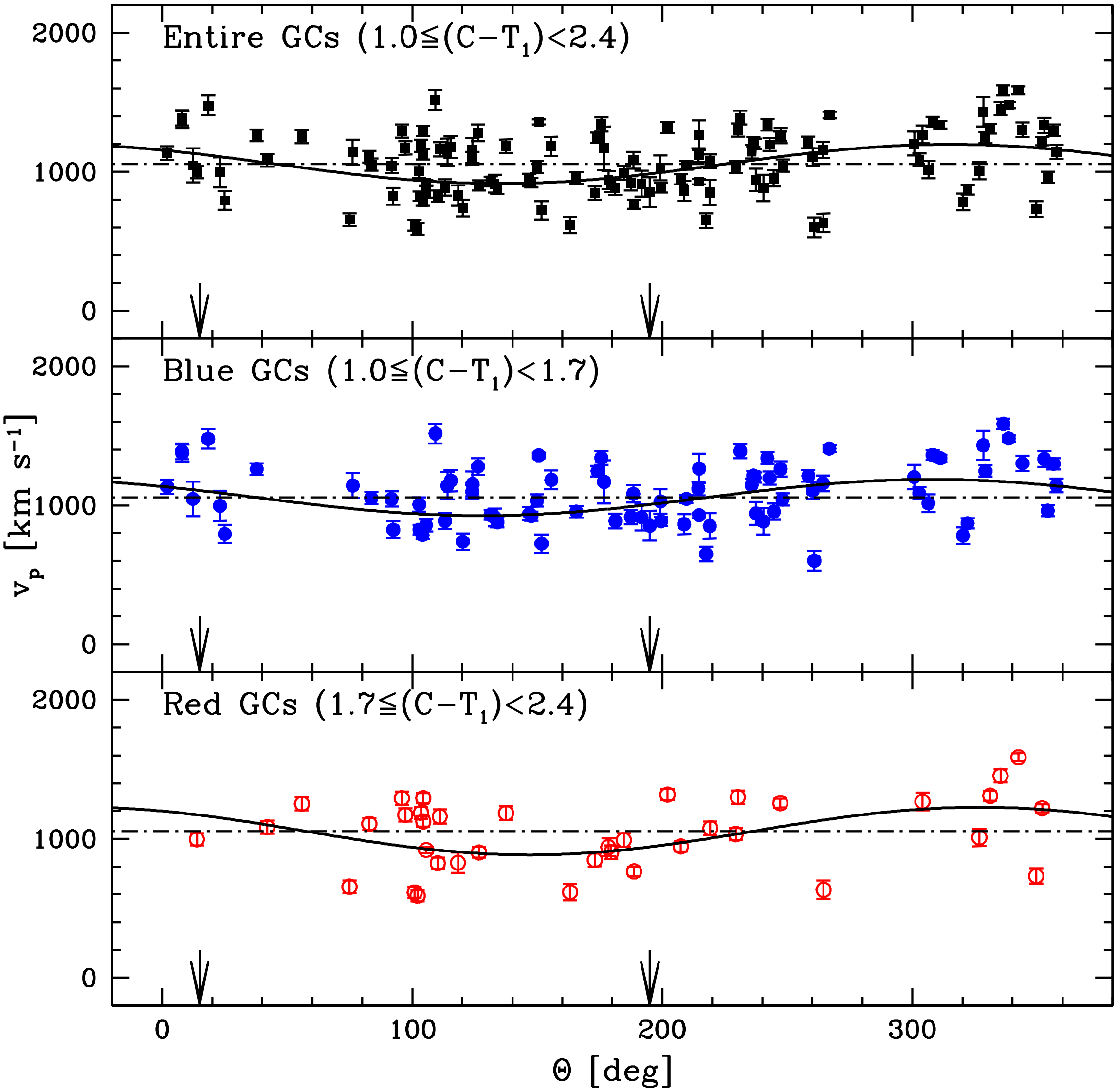

Fig. 2.— Radial velocities versus position angles for entire 121 GCs (top panel), 83 blue GCs (middle panel), and 38 red GCs (bottom panel). The solid curve represents the best fit rotation curve from Table 1, and the dot-dashed horizontal line indicates the systemic velocity of M60. The photometric minor axis of M60 is represented by the vertical arrows ($\Theta = 15°$ and 195°).

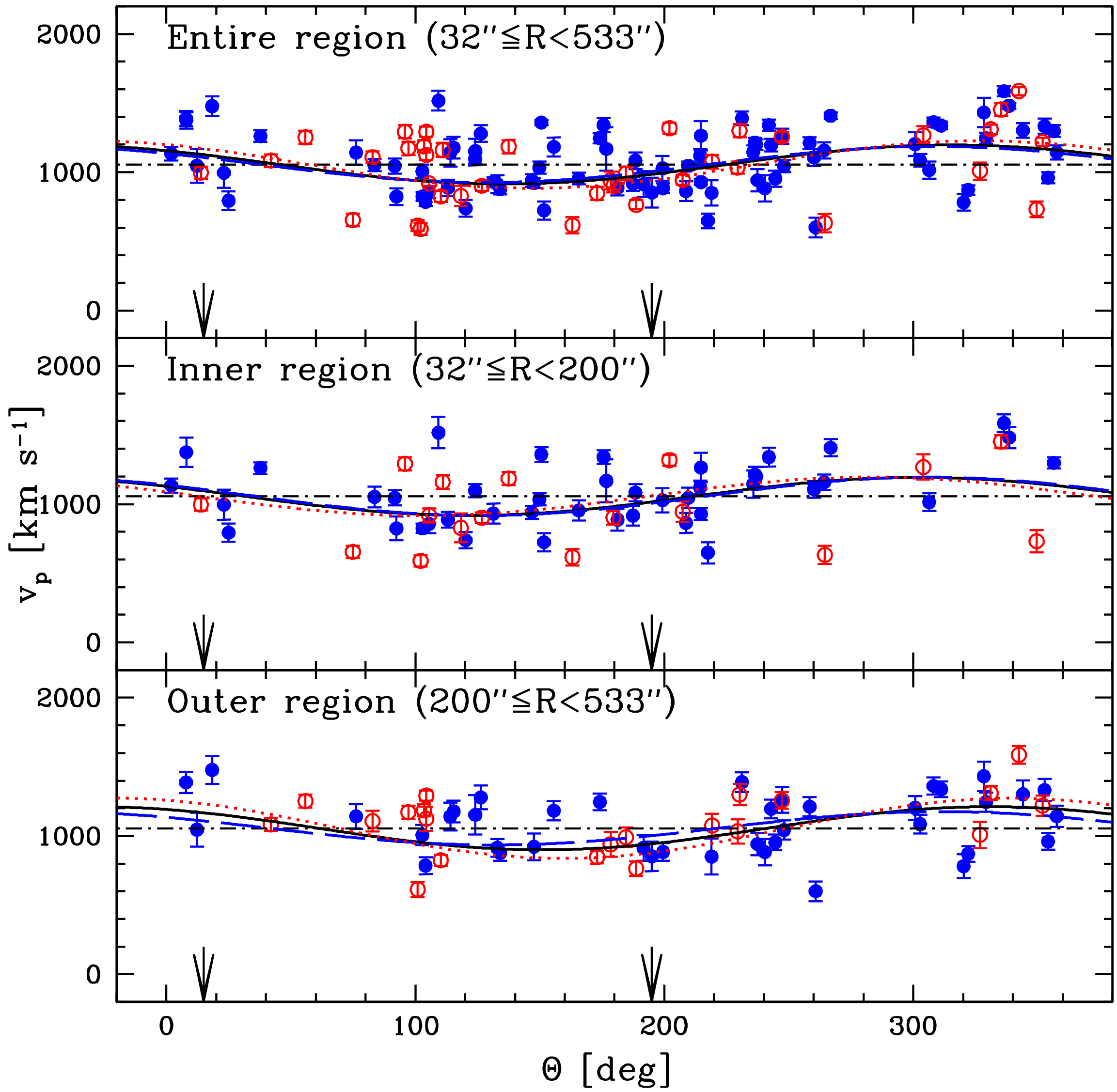

Fig. 3.— Radial velocities versus position angles for the GCs in the range of $32'' \leq R < 533''$ (top panel), $32'' \leq R < 200''$ (middle panel), and $200'' \leq R < 533''$ (bottom panel). Filled circles indicate the blue GCs, while open circles the red GCs. The best fit rotation curves for the entire (solid curves), blue (dashed curves) and red (dotted curves) GCs within each region are overlaid. The dot-dashed horizontal line indicates the systemic velocity of M60, and the vertical arrows mark the position angle of photometric minor axis of M60.

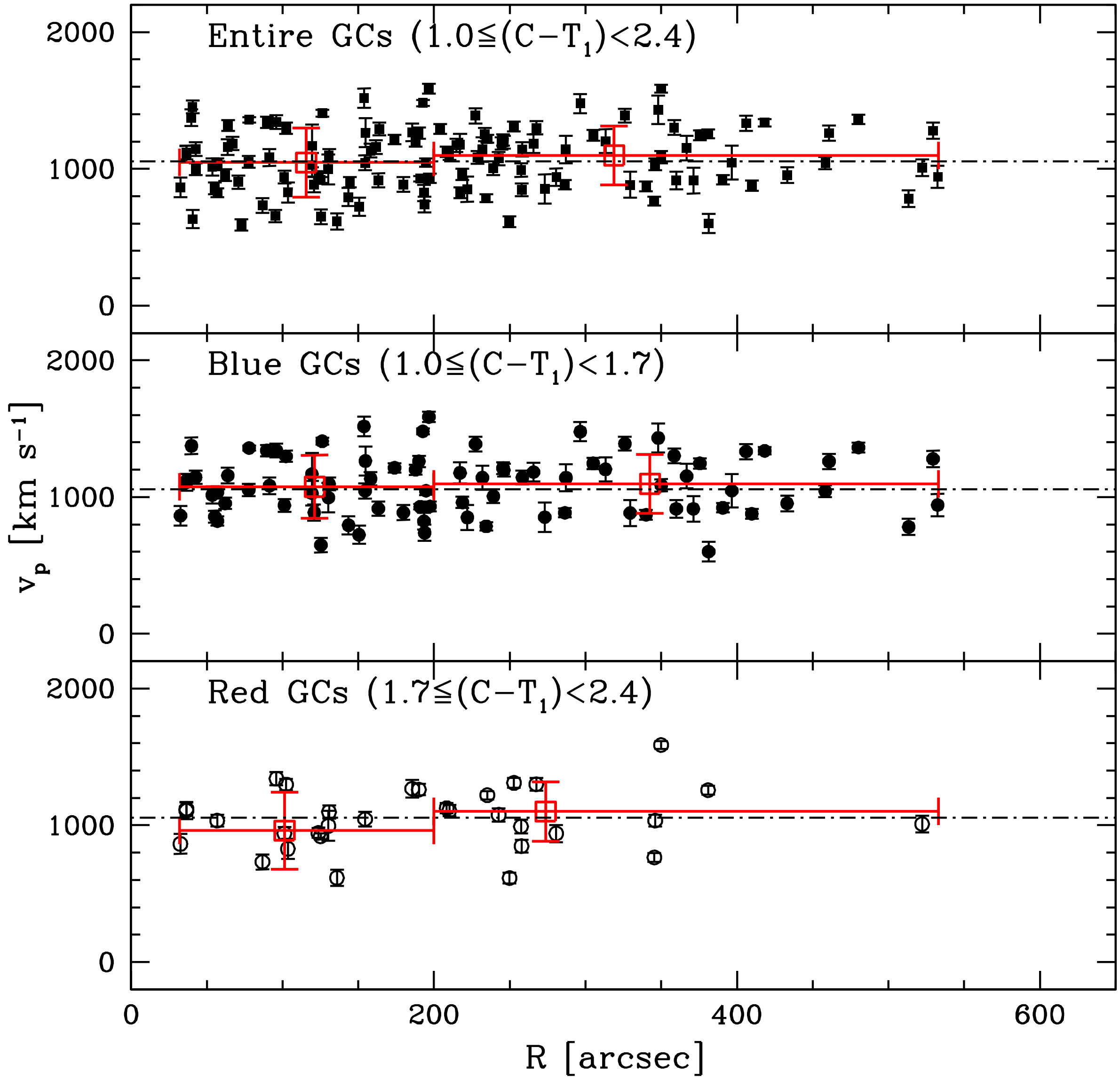

Fig. 4.— Radial velocities versus projected galactocentric distances for the entire (top panel), blue (middle panel), and red (bottom panel) GCs. Large open squares indicate the mean radial velocities of GCs in the radial bins that are represented by long horizontal errorbars. Their vertical errorbars denote the velocity dispersions of GCs in the radial bins. The dot-dashed horizontal line indicates the systemic velocity of M60.

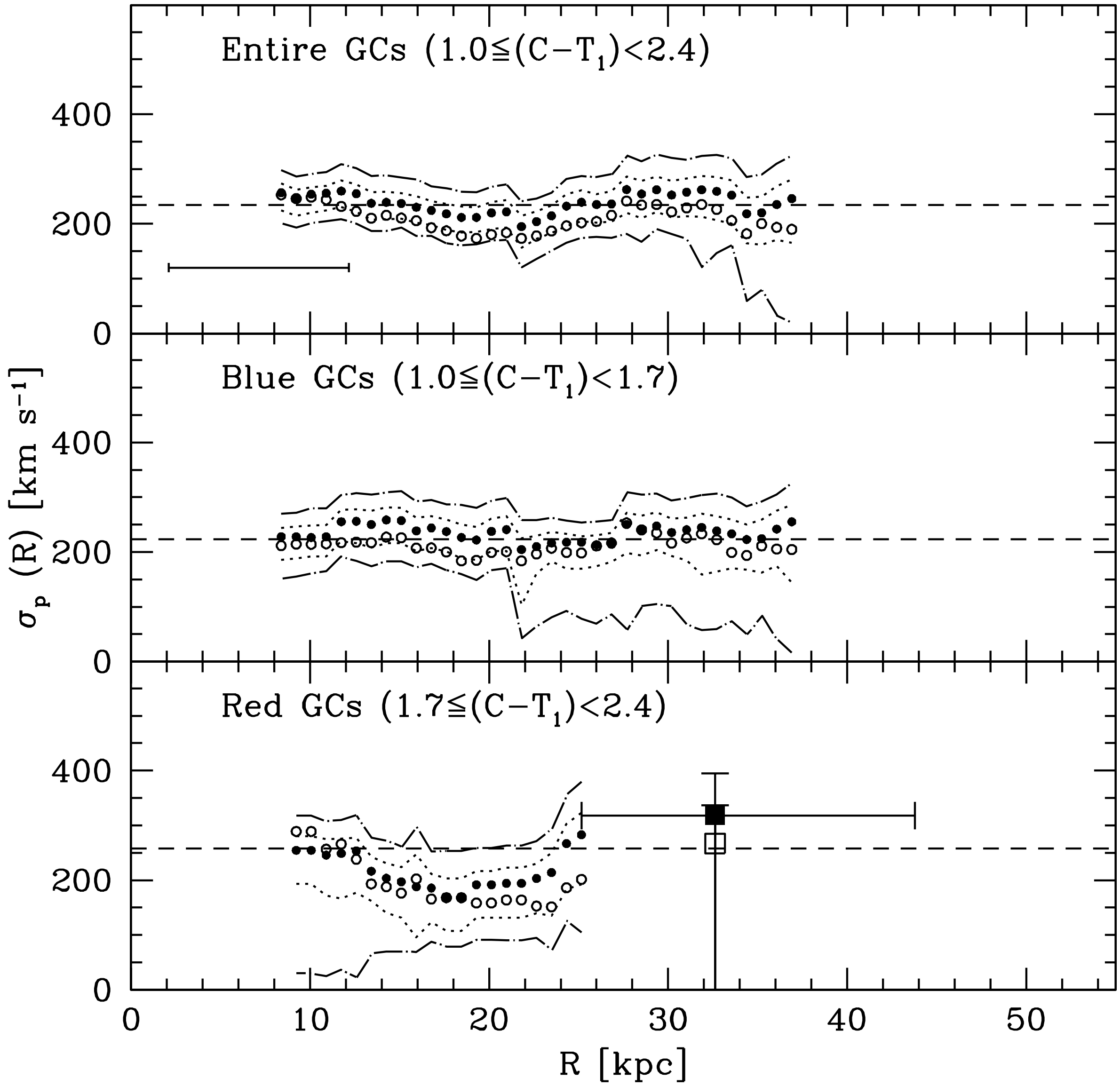

Fig. 5.— Radial profiles of velocity dispersion for the entire (top panel), blue (middle panel), and red (bottom panel) GCs. Filled circles indicate the velocity dispersion about the mean GC velocity ($\sigma_p$) at each point, while open circles the velocity dispersion about the best fit rotation curve ($\sigma_{p,r}$) at the same point. The dispersion is calculated using the GCs within the moving radial bin (width of $2' \simeq 9.77$ kpc) that is represented by a horizontal errorbar in top panel. The dotted and dot-dashed lines denote 68% and 95% confidence intervals on the calculation of velocity dispersion, respectively. The dashed horizontal line indicates the global value of velocity dispersion of GCs in each panel. In the bottom panel, large filled and open squares, respectively, represent the velocity dispersion about the mean GC velocity ($\sigma_p$) and that about the best fit rotation curve ($\sigma_{p,r}$) for the red GCs beyond $R \simeq 25.1$ kpc.

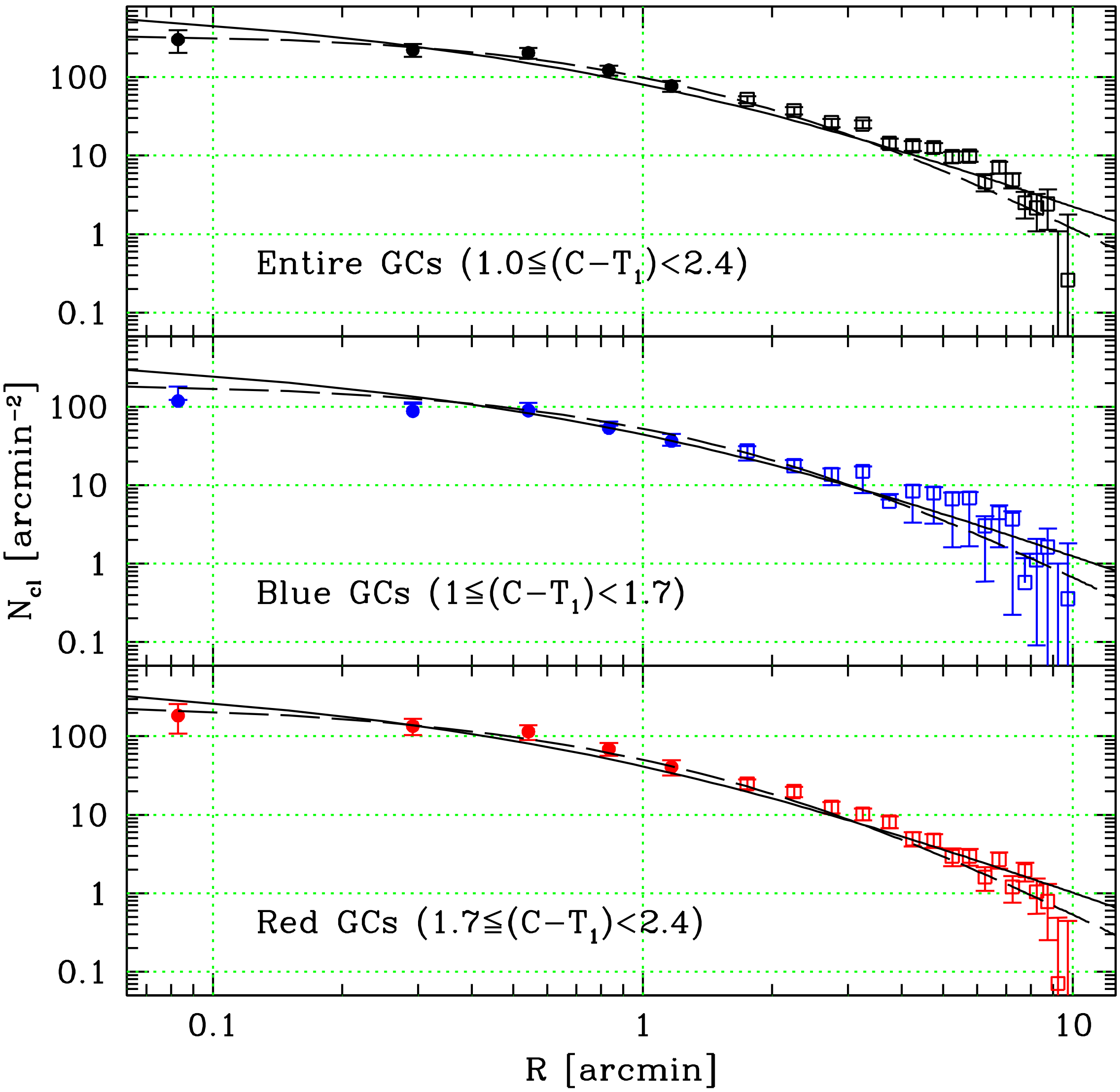

Fig. 6.— Projected number density profiles for the entire (top panel), blue (middle panel), and red (bottom panel) GC candidates. Filled circles represent the GC candidates from HST/WFPC2 archive, while open squares the GC candidates from the KPNO $CT_1$ images (Lee et al. 2007). The solid line and the dashed line in each panel indicate the projected best fits using the NFW density profile and the Dehnen density profile, respectively, for each sample.

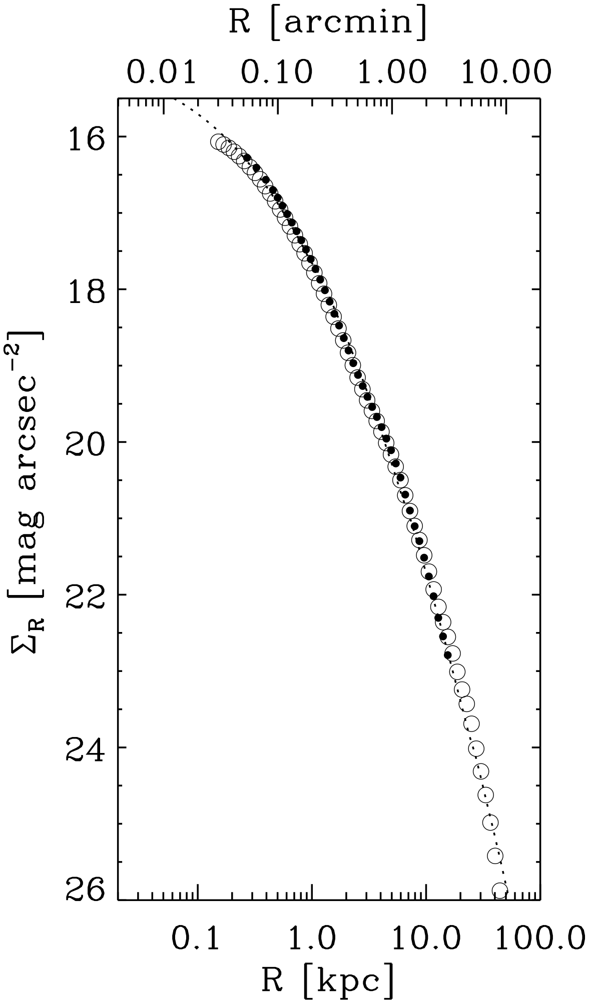

Fig. 7.— *Left*: $R$-band surface photometry of M60 derived from KPNO images (Lee et al. 2007; Kim et al. 2006, open circles) compared to that in Peletier et al. (1990, filled circles). Dashed line indicates a projected best fit using eq. (6). *Right*: Three dimensional stellar mass density profile using the best fit model in the left panel with a constant $R$-band mass-to-light ratio of $\Upsilon_0 = 6.0\ M_\odot L_{R,\odot}^{-1}$.

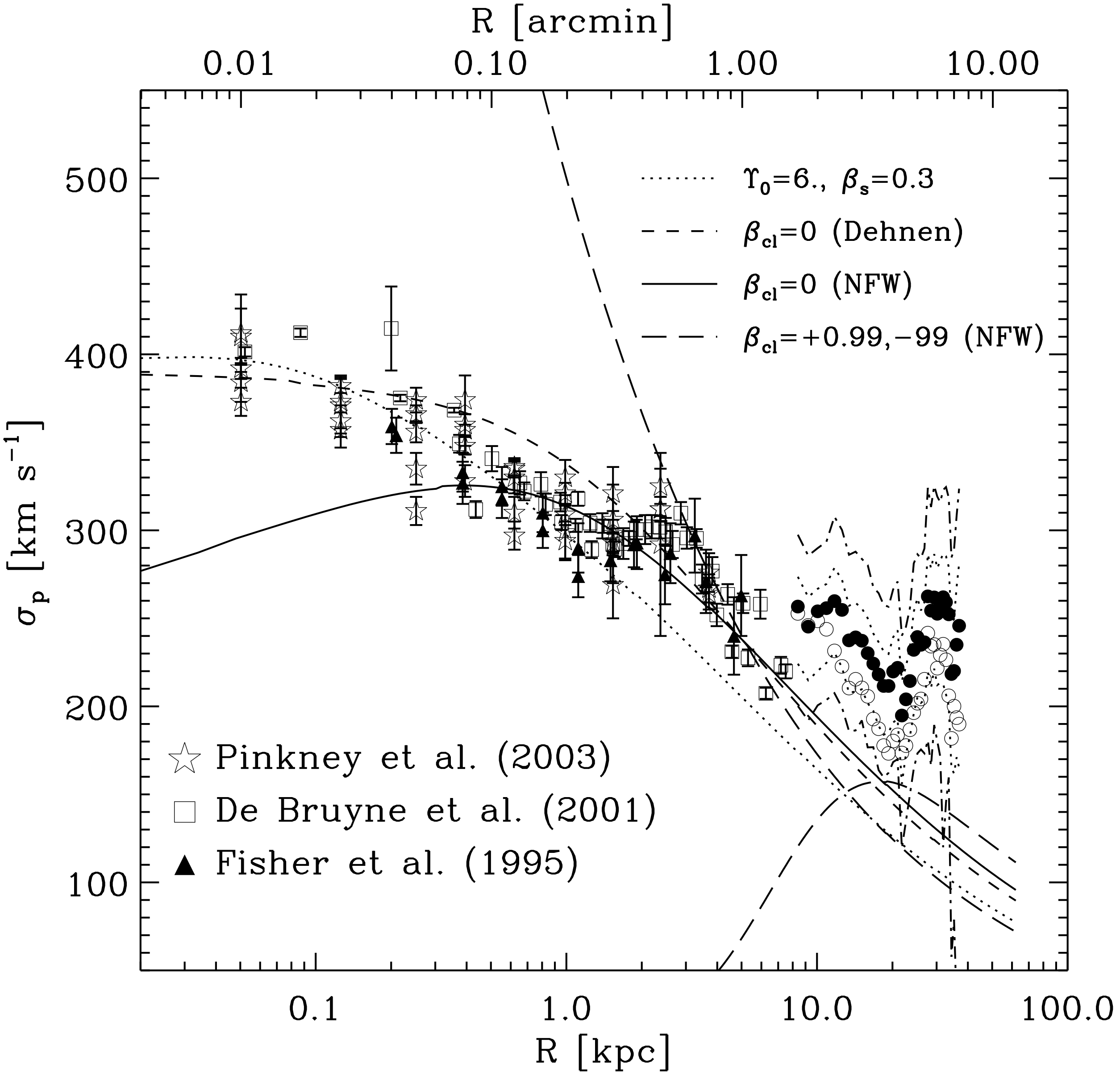

Fig. 8.— VDPs for the stars and the GCs. Stellar VDPs are from Fisher et al. (1995, filled triangles), de Bruyne et al. (2001, open squares), and Pinkney et al. (2003, open stars), and the GC VDPs shown by filled and open circles with associated, dotted and dot-dashed lines are from Fig. 5. Dotted curve represents the stellar VDP calculated using the stellar mass model in Fig. 7 with a constant stellar mass-to-light ratio of $\Upsilon_0 = 6.0\ M_\odot L_{R,\odot}^{-1}$ and a stellar velocity anisotropy of $\beta_s = 0.3$. Other lines indicate the VDPs calculated using the same stellar mass model as above with several GC density profiles and velocity anisotropies: Dehnen and $\beta_{cl} = 0.0$ (short dashed line), NFW and $\beta_{cl} = 0.0$ (solid line), NFW and $\beta_{cl} = +0.99, -99$ (long dashed lines).

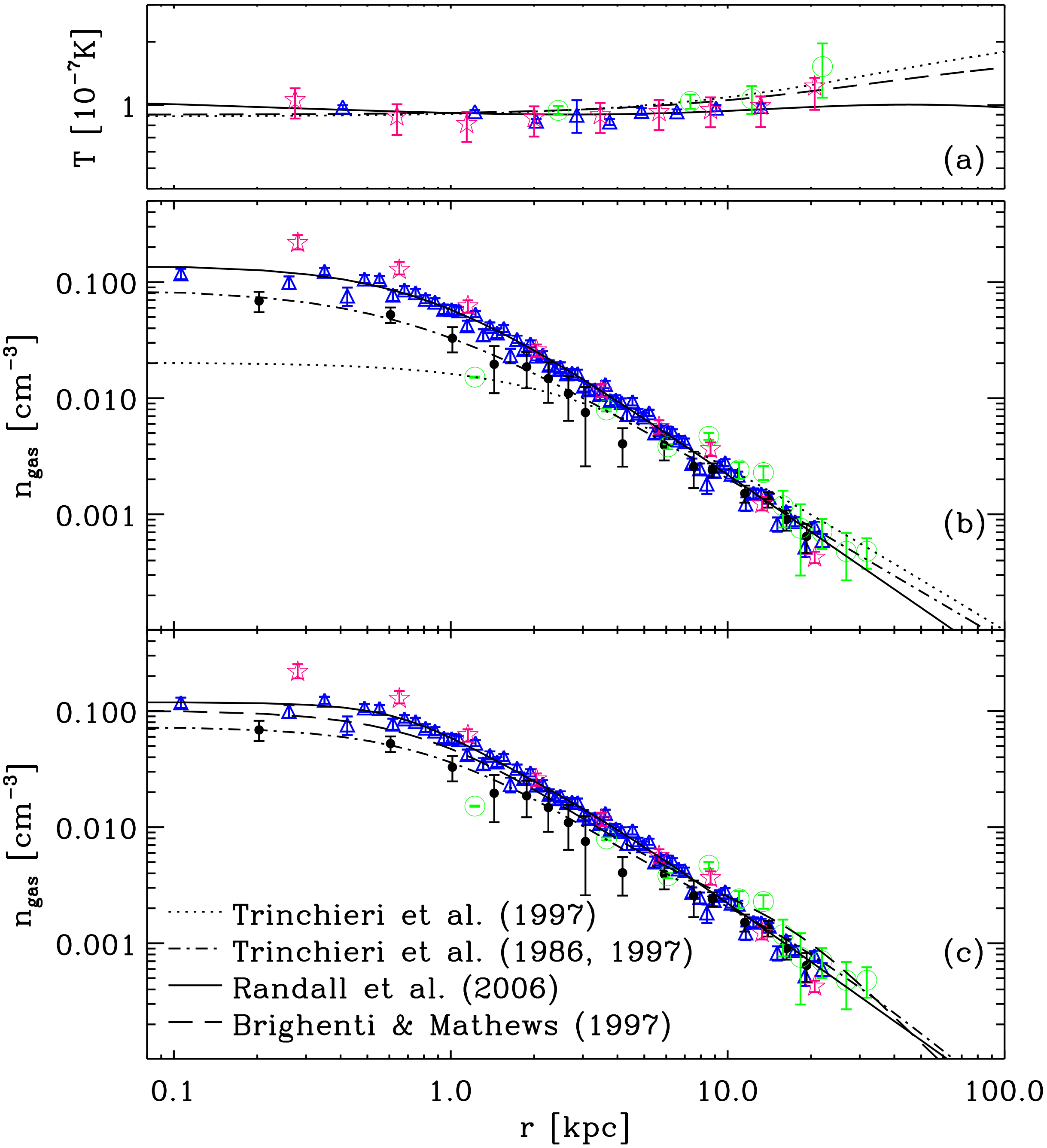

Fig. 9.— Radial profiles of the gas temperature (a), the gas number density with one component fit (b), and the gas number density with two component fit (c). The different symbols represent the data from different literature: Trinchieri et al. (1997, open circles), Trinchieri et al. (1986, filled circles), Randall et al. (2006, open triangles), and Humphrey et al. (2006, open stars). The dotted, dot-dashed and solid lines in each panel indicate the best fit curves using the annotated data, while the long dashed lines in (a) and (c) denote the profiles derived by Brighenti & Mathews (1997).

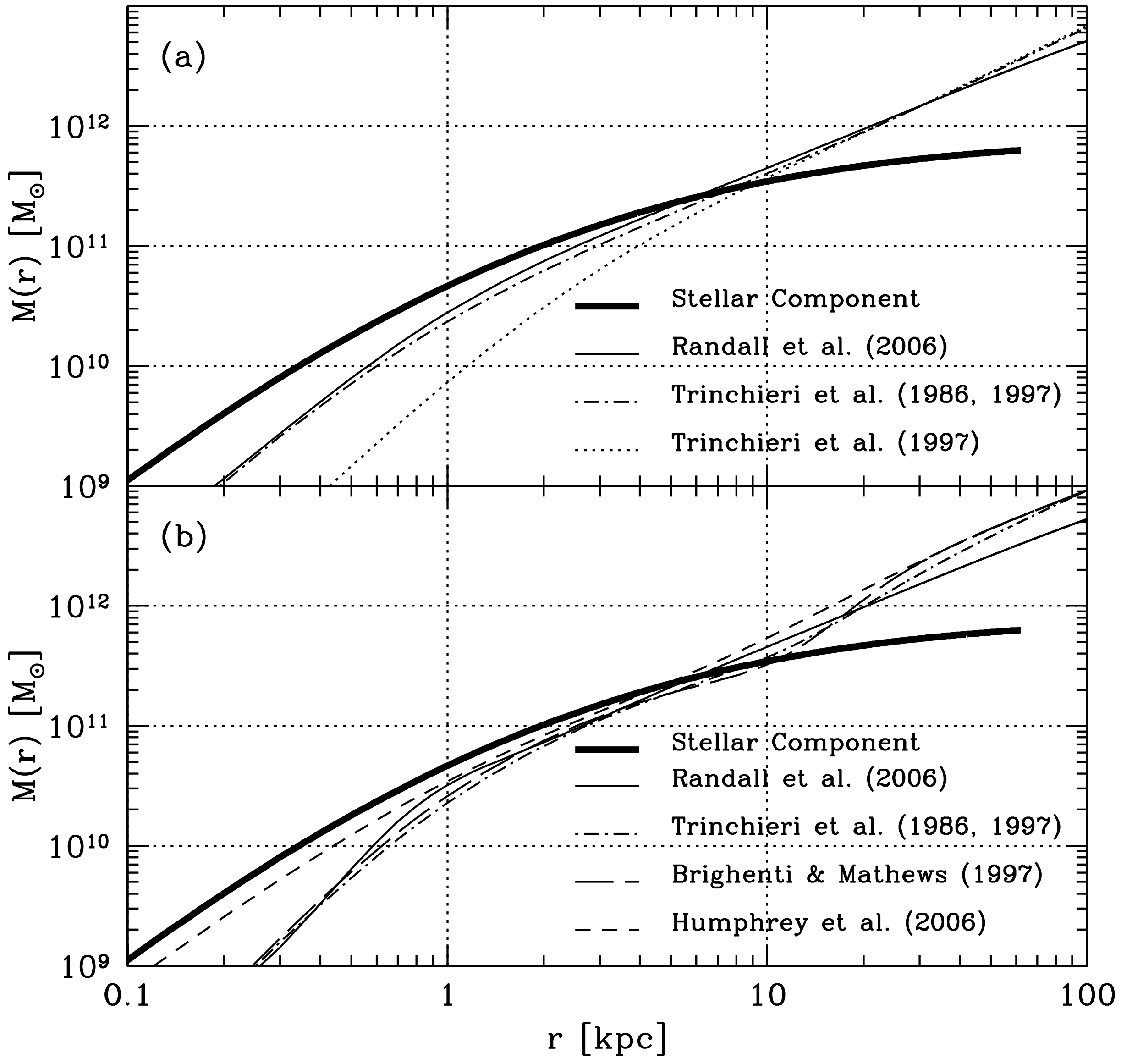

Fig. 10.— Total mass profiles of M60 derived (a) using the gas number density profile with one component fit, and (b) using the gas number density profile with two component fit. The solid, dot-dashed and dotted lines indicate the mass profiles derived in this study using the annotated data, while the long dashed line and the short dashed line in (b) denote the M60 mass profiles derived by Brighenti & Mathews (1997) and Humphrey et al. (2006), respectively. A heavy solid line represents the stellar mass profile using a constant *R*-band mass-to-light ratio of $\Upsilon_0 = 6.0\ M_\odot L_{R,\odot}^{-1}$ derived in §3.3.2.

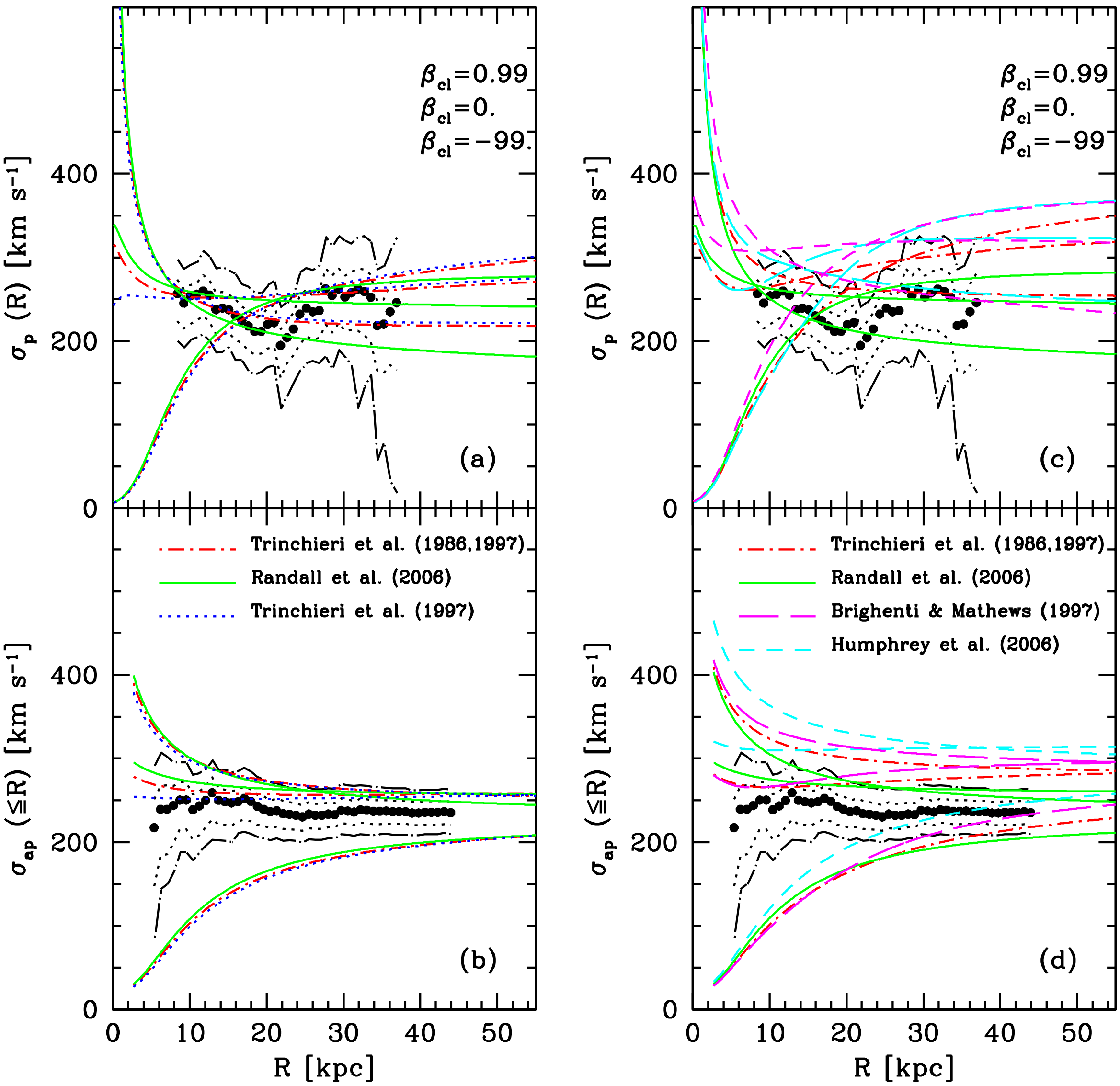

Fig. 11.— VDPs (a, c) and the aperture VDPs (b, d) for the entire GCs. Filled circles in (a, c) represent the measured VDP shown in Fig. 5, and those in (b, d) denote the measured aperture VDP. Associated, dotted and dot-dashed lines represent 68% and 95% confidence intervals on the calculation of velocity dispersion, respectively. Three smoothly curved lines, from a radially biased velocity anisotropy to the tangentially biased velocity anisotropy (from top to bottom, $\beta_{\rm cl}$= 0.99, 0, and −99), represent the VDPs calculated using the GC density profile of Dehnen with one component fit of the gas number density profile (a, b) and with two component fit of the gas number density profile (c, d).

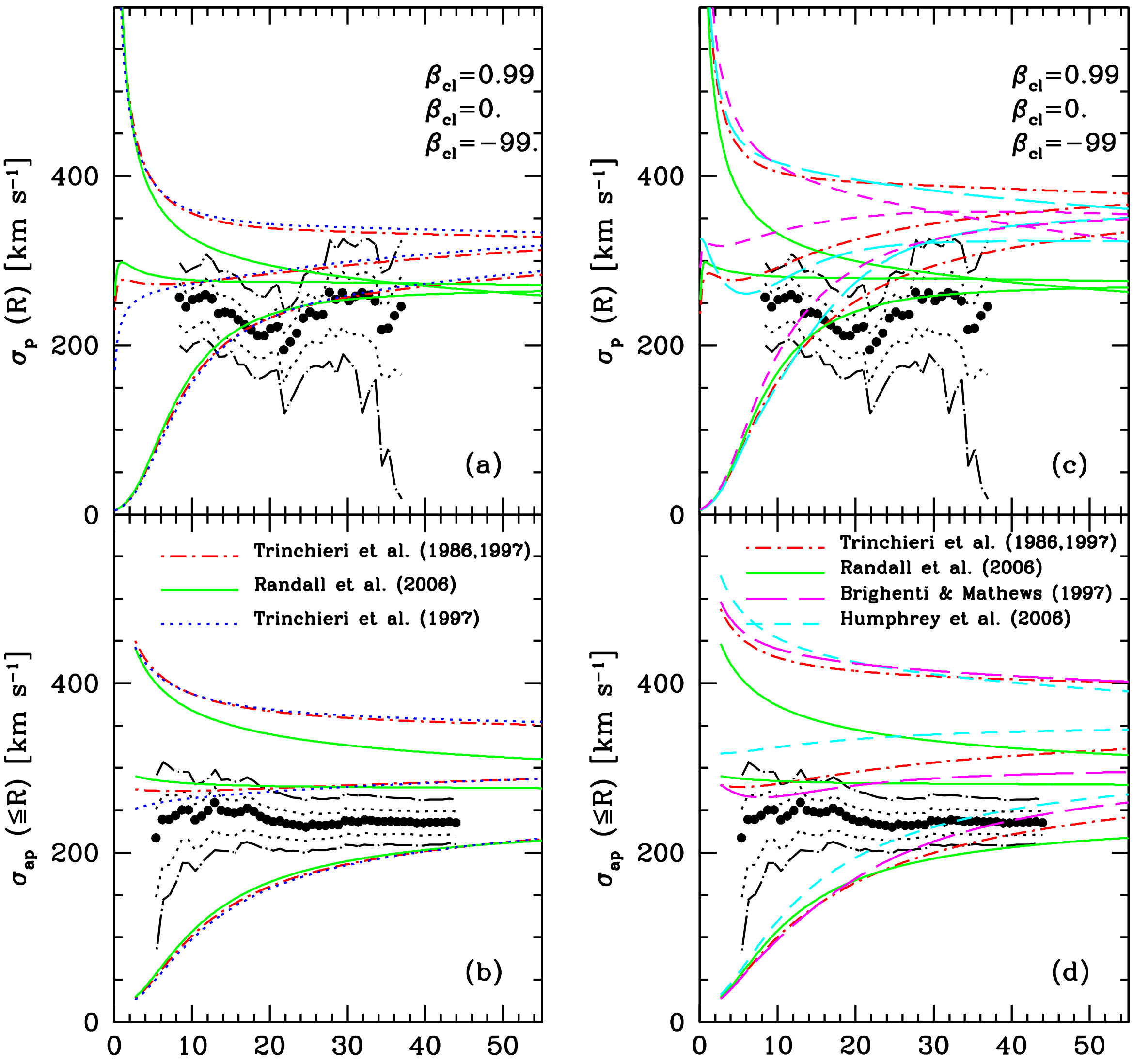

Fig. 12.— Same as Figure 11, but for the VDPs calculated using the GC density profile of NFW.

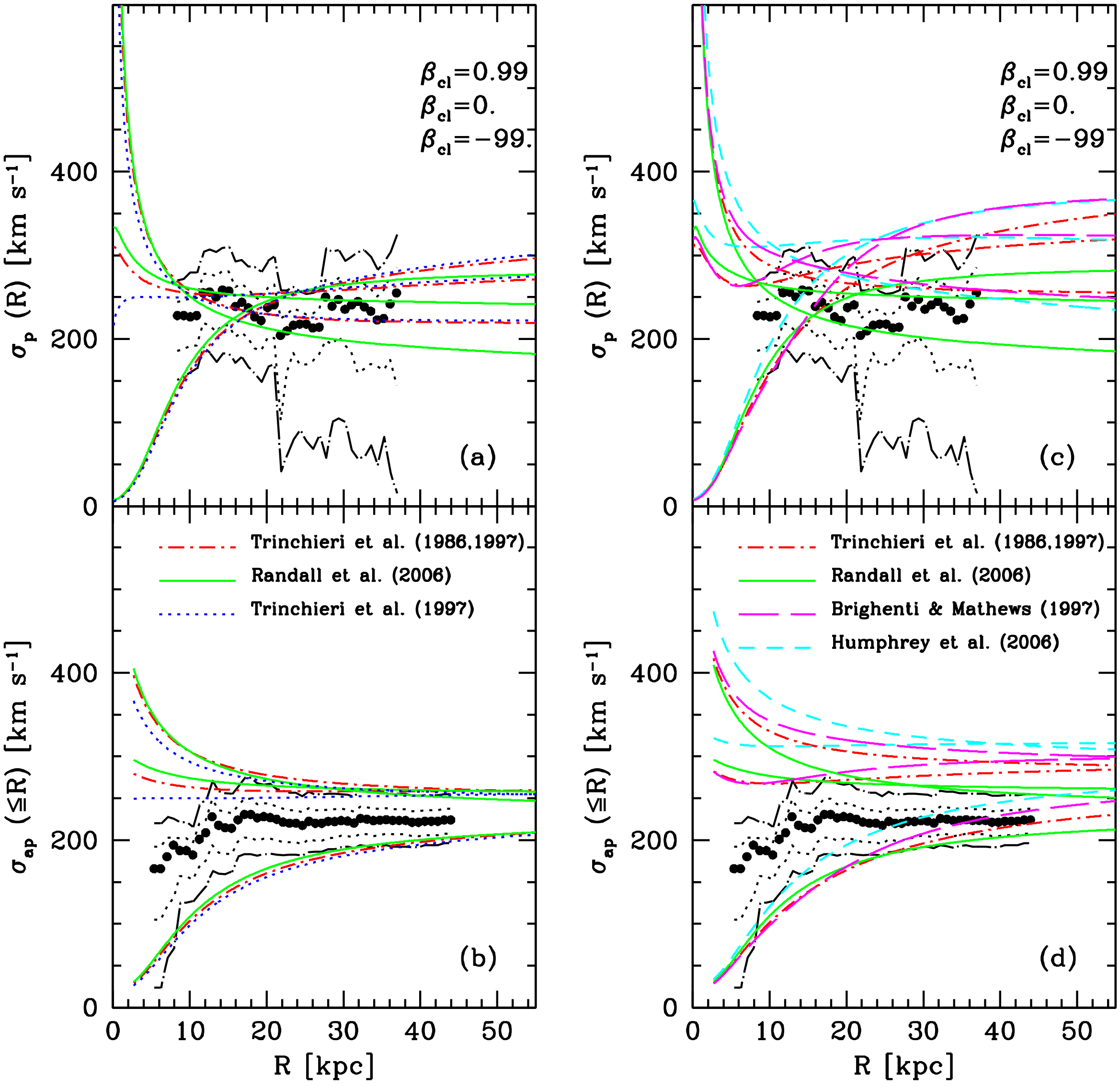

Fig. 13.— Same as Figure 11, but for the blue GCs.

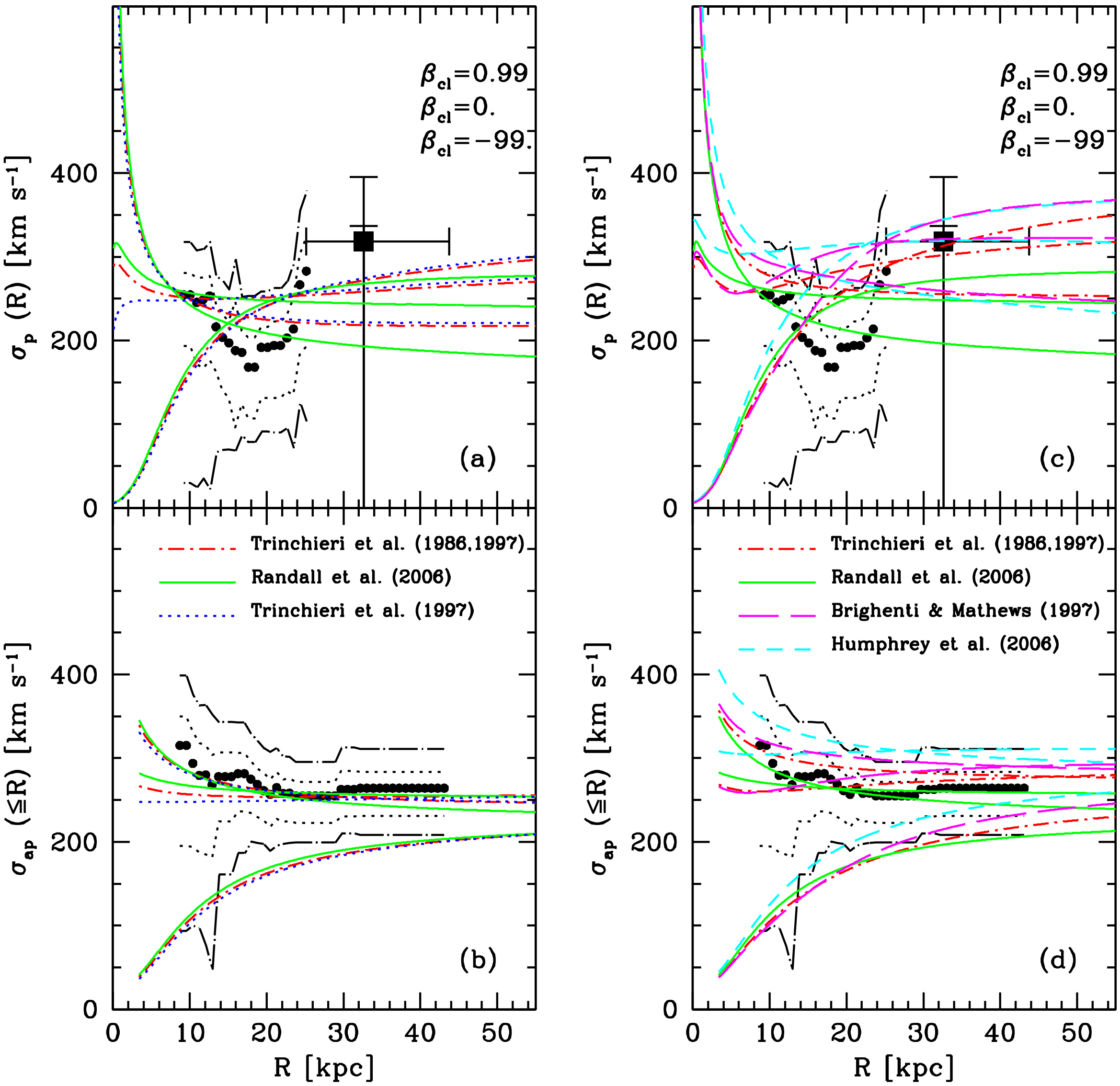

Fig. 14.— Same as Figure 11, but for the red GCs. In the top panels, large filled square represents the measured velocity dispersion about the mean GC velocity ($\sigma_p$) beyond $R \simeq$ 25.1 kpc.

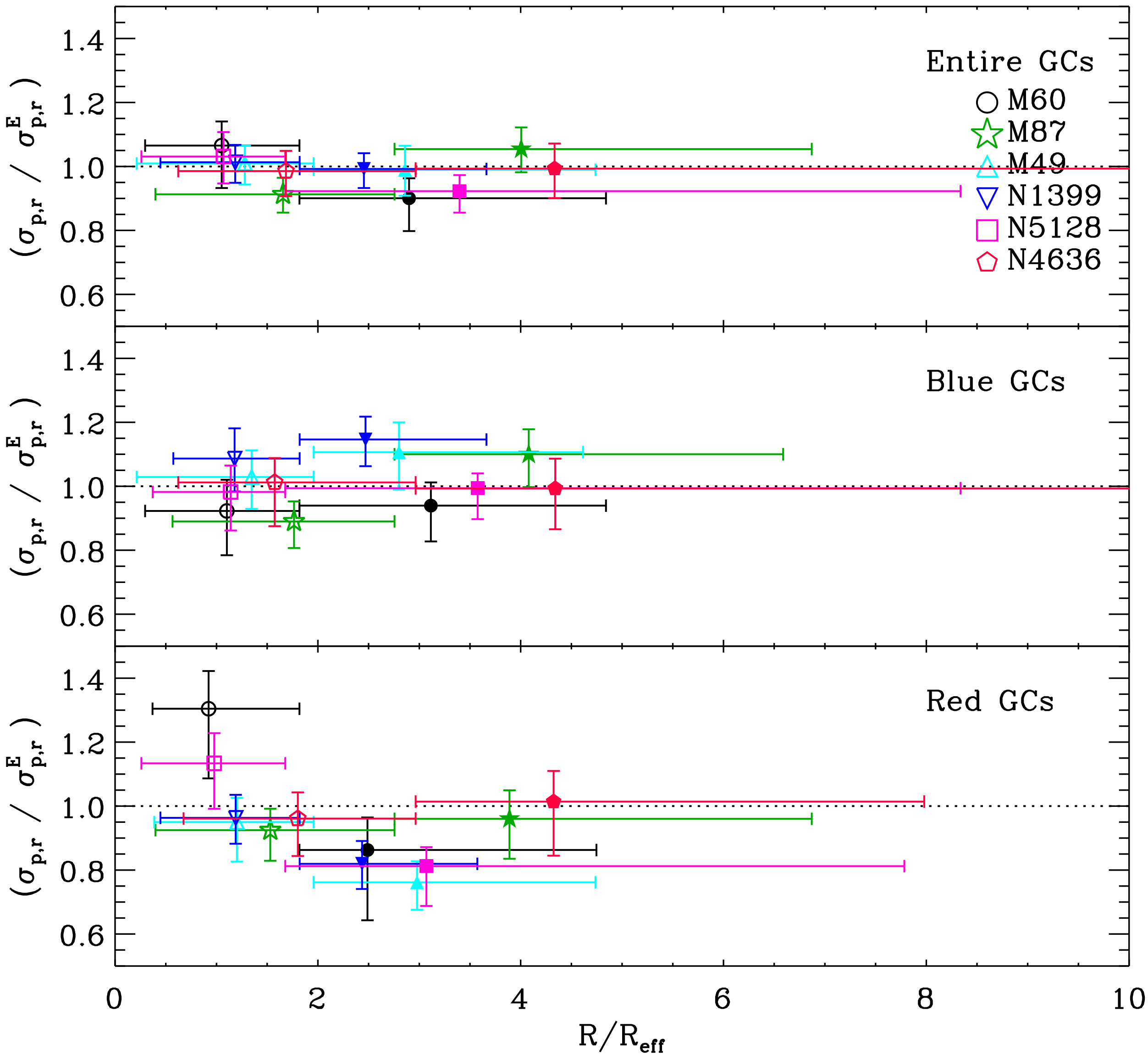

Fig. 15.— Rotation-corrected velocity dispersions in gEs versus the projected galactocentric distances for the entire (top panel), blue (middle panel), and red (bottom panel) GCs. The rotation-corrected velocity dispersion is normalized with respect to that of the entire GCs in each gE. The projected galactocentric distance is normalized with respect to the effective radius of each gE. Open symbols indicate the dispersions in the inner region of each gE, while filled symbols those in the outer region.

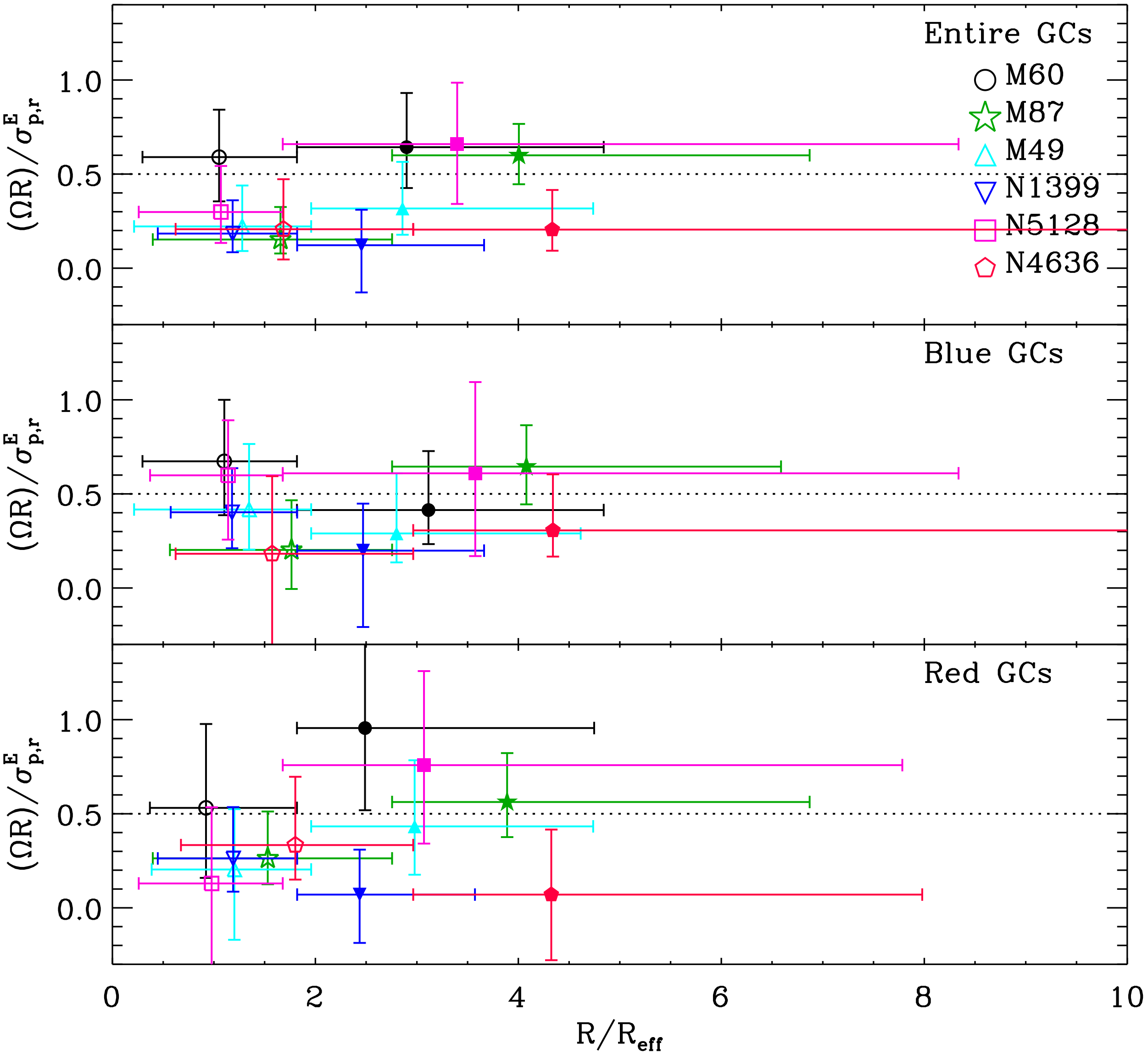

Fig. 16.— Absolute values of the ratio of rotation amplitude to velocity dispersion versus the projected galactocentric distances for the entire (top panel), blue (middle panel), and red (bottom panel) GCs. Open symbols indicate the ratios in the inner region of each gE, while filled symbols those in the outer region.

Table 1. Kinematics of the M60 Globular Cluster System

| $R$ (arcsec) | $\langle R \rangle$ (arcsec) | $N$ | $\overline{v_p}$ (km s$^{-1}$) | $\sigma_p$ (km s$^{-1}$) | $\Theta_0$ (deg) | $\Omega R$ (km s$^{-1}$) | $\sigma_{p,r}$ (km s$^{-1}$) | $\Omega R/\sigma_{p,r}$ |
|---|---|---|---|---|---|---|---|---|
| Entire GCs: 121 Clusters with $1.0 \leq (C - T_1) < 2.4$ | | | | | | | | |
| 32–533 | 218 | 121 | $1073^{+22}_{-22}$ | $234^{+13}_{-14}$ | $225^{+12}_{-14}$ | $141^{+50}_{-38}$ | $217^{+14}_{-16}$ | $0.65^{+0.27}_{-0.22}$ |
| 32–200 | 116 | 60 | $1046^{+37}_{-35}$ | $252^{+15}_{-26}$ | $212^{+18}_{-25}$ | $137^{+83}_{-48}$ | $230^{+17}_{-29}$ | $0.60^{+0.40}_{-0.28}$ |
| 200–533 | 319 | 61 | $1098^{+33}_{-29}$ | $217^{+15}_{-21}$ | $241^{+16}_{-13}$ | $156^{+47}_{-38}$ | $199^{+15}_{-23}$ | $0.78^{+0.30}_{-0.28}$ |
| Blue GCs: 83 Clusters with $1.0 \leq (C - T_1) < 1.7$ | | | | | | | | |
| 32–533 | 228 | 83 | $1086^{+27}_{-25}$ | $223^{+13}_{-16}$ | $218^{+16}_{-23}$ | $130^{+62}_{-51}$ | $207^{+15}_{-19}$ | $0.63^{+0.35}_{-0.30}$ |
| 32–200 | 121 | 43 | $1076^{+37}_{-41}$ | $230^{+19}_{-28}$ | $216^{+18}_{-33}$ | $139^{+119}_{-69}$ | $199^{+21}_{-30}$ | $0.70^{+0.67}_{-0.45}$ |
| 290–533 | 343 | 40 | $1097^{+39}_{-35}$ | $216^{+17}_{-22}$ | $221^{+28}_{-26}$ | $121^{+51}_{-35}$ | $212^{+19}_{-27}$ | $0.57^{+0.29}_{-0.24}$ |
| Red GCs: 38 Clusters with $1.7 \leq (C - T_1) < 2.4$ | | | | | | | | |
| 32–533 | 197 | 38 | $1040^{+48}_{-42}$ | $258^{+21}_{-31}$ | $237^{+18}_{-19}$ | $171^{+58}_{-46}$ | $240^{+20}_{-34}$ | $0.71^{+0.30}_{-0.29}$ |
| 32–200 | 102 | 17 | $961^{+72}_{-78}$ | $282^{+25}_{-45}$ | $193^{+40}_{-37}$ | $139^{+94}_{-44}$ | $281^{+25}_{-45}$ | $0.49^{+0.38}_{-0.24}$ |
| 200–533 | 274 | 21 | $1100^{+55}_{-46}$ | $219^{+31}_{-55}$ | $249^{+21}_{-18}$ | $218^{+83}_{-68}$ | $186^{+21}_{-40}$ | $1.17^{+0.58}_{-0.62}$ |

## Table 2. Gas Temperature and Number Density

| Data | $T(r)$ | | | | $n(r)$ $(i \leq 1)$ | | | $n(r)$ $(i \leq 2)$ | | |
|---|---|---|---|---|---|---|---|---|---|---|
| | $T_m$ ($10^7$ K) | $r_m$ (kpc) | $r_{ot}$ (kpc) | q | $n_0(1)$ ($\mathrm{cm}^{-3}$) | $r_0(1)$ (kpc) | p(1) | $n_0(1)$, $n_0(2)$ ($\mathrm{cm}^{-3}$) | $r_0(1)$, $r_0(2)$ (kpc) | p(1), p(2) |
| T97 [a] | 1.16 | 37.32 | 23.03 | $-0.003$ | 0.02 | 2.60 | 1.45 | ... | ... | ... |
| T97+T86 [b] | ... | ... | ... | ... | 0.09 | 0.70 | 1.41 | 0.07, 0.0009 | 0.97, 16.83 | 1.69, 2.22 |
| R06 [c] | 7.47 | 19.49 | 17.34 | 0.19 | 0.14 | 0.81 | 1.65 | 0.06, 0.05 | 0.81, 1.61 | 3.08, 1.71 |
| BM97 [d] | 0.9 | 24.28 | 24.28 | 0.0 | ... | ... | ... | 0.1, 0.0014 | 0.9, 18.21 | 1.8, 3.0 |

[a] Trinchieri et al. (1997).

[b] Trinchieri et al. (1997) and Trinchieri et al. (1986).

[c] Randall et al. (2006).

[d] Values taken from Brighenti & Mathews (1997).

Table 3. Giant Elliptical Galaxy Samples

| Galaxy | $M_V$ [a] | $\mathrm{v}_{sys}$ [b] (km $s^{-1}$) | $R_{\rm eff}$ [c] (kpc) | $\epsilon$ [d] | $\mathrm{PA}_{\rm minor}$ [c] (deg) | Distance [e] (Mpc) |
|---|---|---|---|---|---|---|
| M60 | −22.44 | 1056 | 9.23 | 0.21 | 15 | 17.3 |
| M87 | −22.62 | 1307 | 7.66 | 0.125 | 69 | 17.2 |
| M49 | −22.83 | 997 | 9.97 | 0.175 | 65 | 17.1 |
| NGC 1399 | −21.95 | 1442 | 14.55 | 0.099 | 20 | 20.0 |
| NGC 5128 | −21.66 | 541 | 6.02 | 0.224 | 125 | 4.2 |
| NGC 4636 | −21.43 | 906 | 6.37 | 0.256 | 58 | 14.7 |

[a] Absolute $V$ magnitude based on $B_T$, $(B-V)_T$ (de Vaucouleurs et al. 1991), $A_V$ (Schlegel et al. 1998), and distance adopted in this study.

[b] M60 (This study), M87, M49 (Smith et al. 2000), NGC 1399 (Richtler et al. 2004), NGC 5128 (Hui et al. 1995), and NGC 4636 (Schuberth et al. 2006).

[c] Position angle of the minor axis. M60 (Lee et al. 2007), NGC 5128 (Dufour et al. 1979), and other galaxies (Kim et al. 2006).

[d] M60 (Lee et al. 2007), NGC 5128 (de Vaucouleurs et al. 1991) and other galaxies (Kim et al. 2006).

[e] M60, M87, and M49 (Mei et al. 2007), and other galaxies (Tonry et al. 2001).

Table 4. Global Kinematic Properties of GCs in gEs

| Galaxy | GC | $N$ | $\overline{v_p}$ (km s$^{-1}$) | $\sigma_p$ (km s$^{-1}$) | $\Theta_0$ (deg) | $\Omega R$ (km s$^{-1}$) | $\sigma_{p,r}$ (km s$^{-1}$) | $\Omega R/\sigma_{p,r}$ |
|---|---|---|---|---|---|---|---|---|
| M60 | EGC | 121 | $1073^{+22}_{-22}$ | $234^{+13}_{-14}$ | $225^{+12}_{-14}$ | $141^{+50}_{-38}$ | $217^{+14}_{-16}$ | $0.65^{+0.27}_{-0.22}$ |
| | BGC | 83 | $1086^{+27}_{-25}$ | $223^{+13}_{-16}$ | $218^{+16}_{-23}$ | $130^{+62}_{-51}$ | $207^{+15}_{-19}$ | $0.63^{+0.35}_{-0.30}$ |
| | RGC | 38 | $1040^{+48}_{-42}$ | $258^{+21}_{-31}$ | $237^{+18}_{-19}$ | $171^{+58}_{-46}$ | $240^{+20}_{-34}$ | $0.71^{+0.30}_{-0.29}$ |
| M87 | EGC | 276 | $1333^{+25}_{-23}$ | $414^{+15}_{-18}$ | $68^{+11}_{-12}$ | $172^{+39}_{-28}$ | $399^{+15}_{-18}$ | $0.43^{+0.12}_{-0.09}$ |
| | BGC | 158 | $1341^{+36}_{-33}$ | $425^{+22}_{-25}$ | $59^{+17}_{-17}$ | $181^{+57}_{-44}$ | $414^{+22}_{-26}$ | $0.44^{+0.16}_{-0.13}$ |
| | RGC | 118 | $1324^{+39}_{-37}$ | $400^{+25}_{-28}$ | $79^{+16}_{-17}$ | $165^{+53}_{-33}$ | $380^{+24}_{-27}$ | $0.43^{+0.17}_{-0.12}$ |
| M49 | EGC | 263 | $973^{+20}_{-18}$ | $322^{+14}_{-17}$ | $106^{+44}_{-45}$ | $54^{+50}_{-23}$ | $321^{+14}_{-17}$ | $0.17^{+0.17}_{-0.08}$ |
| | BGC | 159 | $954^{+32}_{-27}$ | $352^{+21}_{-25}$ | $102^{+36}_{-37}$ | $92^{+71}_{-35}$ | $349^{+21}_{-24}$ | $0.27^{+0.22}_{-0.12}$ |
| | RGC | 104 | $999^{+31}_{-25}$ | $276^{+19}_{-23}$ | $182^{+53}_{-50}$ | $11^{+79}_{-83}$ | $278^{+19}_{-23}$ | $0.04^{+0.29}_{-0.30}$ |
| NGC 1399 | EGC | 435 | $1442^{+15}_{-14}$ | $323^{+11}_{-13}$ | $307^{+50}_{-46}$ | $31^{+43}_{-48}$ | $326^{+11}_{-13}$ | $0.10^{+0.14}_{-0.15}$ |
| | BGC | 216 | $1445^{+26}_{-22}$ | $359^{+17}_{-21}$ | $261^{+45}_{-52}$ | $69^{+68}_{-29}$ | $364^{+18}_{-21}$ | $0.19^{+0.20}_{-0.09}$ |
| | RGC | 219 | $1439^{+19}_{-17}$ | $285^{+16}_{-19}$ | $0^{+40}_{-36}$ | $46^{+53}_{-39}$ | $288^{+16}_{-19}$ | $0.16^{+0.19}_{-0.15}$ |
| NGC 5128 | EGC | 210 | $536^{+9}_{-8}$ | $129^{+5}_{-7}$ | $184^{+23}_{-26}$ | $30^{+16}_{-14}$ | $129^{+5}_{-7}$ | $0.23^{+0.14}_{-0.13}$ |
| | BGC | 127 | $526^{+11}_{-11}$ | $126^{+7}_{-8}$ | $168^{+27}_{-47}$ | $25^{+22}_{-35}$ | $129^{+7}_{-7}$ | $0.19^{+0.18}_{-0.29}$ |
| | RGC | 83 | $552^{+16}_{-15}$ | $133^{+9}_{-11}$ | $191^{+40}_{-75}$ | $47^{+43}_{-54}$ | $132^{+9}_{-11}$ | $0.36^{+0.35}_{-0.44}$ |
| NGC 4636 | EGC | 172 | $899^{+16}_{-14}$ | $207^{+10}_{-11}$ | $275^{+47}_{-50}$ | $29^{+35}_{-14}$ | $207^{+10}_{-11}$ | $0.14^{+0.18}_{-0.08}$ |
| | BGC | 96 | $901^{+23}_{-20}$ | $207^{+14}_{-15}$ | $234^{+56}_{-52}$ | $19^{+49}_{-53}$ | $207^{+14}_{-15}$ | $0.09^{+0.25}_{-0.26}$ |
| | RGC | 76 | $896^{+27}_{-24}$ | $208^{+12}_{-17}$ | $289^{+40}_{-42}$ | $50^{+46}_{-21}$ | $208^{+12}_{-18}$ | $0.24^{+0.23}_{-0.12}$ |

Table 5. Summary of Global Kinematic Properties of GCs in gEs

| Galaxy | Velocity Dispersion | GC | Rotation | Rotation Axis | $\beta_{cl}$ [a] |
|---|---|---|---|---|---|
| M60 | $\sigma_{p,r}(BGC) \lesssim \sigma_{p,r}(RGC)$ | EGC | Strong | Minor Axis | modest tangential |
| | | BGC | Strong | Minor Axis | modest tangential |
| | | RGC | Strong | None | modest radial/isotropic |
| M87 | $\sigma_{p,r}(BGC) \gtrsim \sigma_{p,r}(RGC)$ | EGC | Strong | Minor Axis | isotropic |
| | | BGC | Strong | Minor Axis | modest tangential |
| | | RGC | Strong | Minor Axis | modest radial |
| M49 | $\sigma_{p,r}(BGC) > \sigma_{p,r}(RGC)$ | EGC | Weak | None | isotropic |
| | | BGC | Modest | None | closely isotropic |
| | | RGC | Weak | Major Axis | closely isotropic |
| NGC 1399 | $\sigma_{p,r}(BGC) > \sigma_{p,r}(RGC)$ | EGC | Weak | Major Axis | closely isotropic |
| | | BGC | Weak | Major Axis | closely isotropic |
| | | RGC | Weak | Minor Axis | closely isotropic |
| NGC 5128 | $\sigma_{p,r}(BGC) \simeq \sigma_{p,r}(RGC)$ | EGC | Modest | None | – |
| | | BGC | Weak | None | – |
| | | RGC | Modest | Major Axis | – |
| NGC 4636 | $\sigma_{p}(BGC) \simeq \sigma_{p}(RGC)$ | EGC | Weak | None | – |
| | | BGC | Weak | Minor Axis | modest tangential |
| | | RGC | Modest | None | – |

[a] M60 (This study), M87 (Côté et al. 2001), M49 (Côté et al. 2003), NGC 1399 (Richtler et al. 2004), and NGC 4636 (Schuberth et al. 2006).